

A daily highest air temperature estimation method and spatial-temporal changes analysis of high temperature in China from 1979 to 2018

Ping Wang^{1,2}★, Kebiao Mao^{1,3}★, Fei Meng², Zhihao Qin³, Shu Fang⁴, Sayed M. Bateni⁵, Mansour Almazroui^{6,7}

¹ School of Physics and Electronic-Engineering, Ningxia University, Yinchuan 750021, China

² School of Surveying and Geo-Informatics, Shandong Jianzhu University, Jinan 250100, China

³ Institute of agricultural resources and regional planning, Chinese Academy of Agricultural Sciences, Beijing 100081, China

⁴ School of Earth Sciences and Resources, China University of Geosciences, Beijing 100083, China

⁵ Department of Civil and Environmental Engineering and Water Resources Research Center, University of Hawaii at Manoa, Honolulu, HI 96822, USA

⁶ Centre of Excellence for Climate Change Research/Department of Meteorology, King Abdulaziz University, Jeddah 21589, Saudi Arabia

⁷ Climatic Research Unit, School of Environmental Sciences, University of East Anglia, Norwich, UK

Correspondence to: Kebiao Mao (maokebiao@caas.cn)

★ These authors contributed equally to this works.

Abstract. The daily highest air temperature (T_{\max}) is a key parameter for global and regional high temperature analysis, which is very difficult to be obtained in areas where there are no meteorological observation stations. This study proposes an estimation framework for obtaining high-precision T_{\max} . Firstly, we build a near surface air temperature diurnal variation model to estimate T_{\max} for China from 1979 to 2018 based on multi-source data. Then in order to further improve the estimation accuracy, we divided China into six regions according to climate conditions and topography, and established calibration models for different regions. The analysis shows that the mean absolute error (MAE) of the dataset (<https://doi.org/10.5281/zenodo.6322881>) is about 1.07 °C and RMSE is 1.52 °C, which improves the accuracy of the traditional method by nearly 1 °C. The spatial-temporal variations analysis of T_{\max} in China indicated that the annual and seasonal mean T_{\max} in most areas of China showed an increasing trend. In summer and autumn, the T_{\max} in

30 northeast China increased the fastest among the six regions, which were 0.4°C/10a and 0.39°C/10a,
31 respectively. The number of summer days and warm days showed an increasing trend in all regions,
32 while the number of icing days and cold days showed a decreasing trend. The abnormal temperature
33 changes mainly occurred in El Niño years or La Niña years. We found that the influence of the
34 Indian Ocean Basin Warming (IOBW) on air temperature in China were generally greater than those
35 of the North Atlantic Oscillation and the NINO3.4 area sea surface temperature after making
36 analysis of ocean climate modal indices with air temperature. In general, this T_{\max} dataset and
37 analysis are of great significance to the study of climate change in China, especially for
38 environmental protection.

39 **Keywords:** Near surface air temperature diurnal variation model; Daily highest air temperature; High temperature;
40 Spatial-temporal analysis; Climate change

41 **1 Introduction**

42 In the context of global warming, the frequency of high temperature events is increasing, and high
43 temperature tends to increase electricity demand and energy consumption (Zhang et al., 2021;
44 Sathaye et al., 2013), adversely affecting human health, social economy and ecosystem (Sehra et al.,
45 2020; Basu, 2009; Gasparrini and Armstrong, 2011). The daily highest air temperature (T_{\max}) is the
46 basic parameter for studying regional scale high-temperature events. It has a great influence on the
47 ozone concentration (Abdullah et al., 2017; Kleinert et al., 2021) and the start time of the plant
48 growth season on the Tibetan Plateau (Yang et al., 2017). T_{\max} is not only an important factor for
49 high temperature disaster risk assessment, but also a key input parameter for crop growth models
50 and carbon emission models. Sustained and abnormally high T_{\max} will cause high temperature heat
51 damage and adversely affect crop growth. Therefore, it is very important to accurately obtain the

52 temporal and spatial distribution of T_{\max} and study the characteristics of high temperature weather.
53 Generally, T_{\max} is measured on a thermometer in a louvered box 1.5 meters above the ground in the
54 field. Although the T_{\max} measured by this method has high accuracy but not spatial continuity.
55 Therefore, some scholars spatialized the station based T_{\max} through methods such as Kriging
56 interpolation and spline function interpolation. However, the number of meteorological stations is
57 limited, and stations in remote areas and areas with complex terrain are even sparser, which makes
58 the accuracy of T_{\max} obtained by interpolation difficult to meet the requirements of regional scale
59 research in China.

60 In order to obtain information about the spatial distribution of the T_{\max} , many scholars began to
61 use satellite remote sensing to solve this problem. There are three commonly remote sensing
62 methods to estimate T_{\max} . The first method is regression analysis, which uses the correlation
63 between retrieved land surface temperature (LST) and T_{\max} to establish a regression model to
64 estimate T_{\max} (Shen and Leptoukh, 2011; Evrendilek et al., 2012; Lin et al., 2012). The second
65 method is machine learning, which can flexibly estimate T_{\max} in urban areas with complex features
66 (Yoo et al., 2018). The third method is to use a diurnal temperature change model to extend the
67 instantaneous air temperature (T_a) to calculate T_{\max} , either by the Temperature-Vegetation Index
68 (TVX) method (Wloczyk et al., 2011; Zhu et al., 2013), the energy balance method (Sun et al., 2005;
69 Zhu et al., 2017), the atmospheric temperature profile extrapolation method (Fabiola and Mario,
70 2010), or other methods. The above methods of estimating T_{\max} with LST can better reflect the
71 spatial distribution of T_{\max} , but regression analysis and machine learning require sufficient and
72 representative samples, and the established model is not universal. TVX cannot estimate T_a at night
73 and in sparse vegetation areas. Many parameters required by the energy balance method cannot

74 usually be obtained by remote sensing technology. The estimation accuracy of atmospheric
75 temperature profile extrapolation method is greatly affected by the accuracy of the atmospheric
76 temperature profile. Therefore, a new method for estimating T_{\max} needs to be proposed.

77 At present, most researches mainly used the extreme climate indices defined by the Expert Team
78 on Climate Change Detection and Indices (ETCCDI) to analyze the temporal and spatial distribution
79 characteristics of high temperature and its changing laws (Khan et al., 2018; Mcgree et al., 2019;
80 Poudel et al., 2020; Ruml et al., 2017; Salman et al., 2017; Wang et al., 2019; Zhang et al., 2019).
81 Zhou et al. (2016) analyzed the temperature indices changes in China from 1961 to 2010, and the
82 results indicated that the warm extremes in China exhibited an increasing trend. In addition, the
83 researchers analyzed the characteristics of high temperature changes in the Three River Headwaters,
84 Yangtze River Basin, Loess Plateau, Inner Mongolia and Songhua River Basin (Ding et al., 2018;
85 Guan et al., 2015; Sun et al., 2016; Tong et al., 2019; Zhong et al., 2017). In addition to analyzing
86 the temporal and spatial changes of high temperature events, many scholars have also studied the
87 influencing factors of high temperature events. Studies showed that extreme high temperature over
88 China was related to abnormal atmospheric circulation disturbances (You et al., 2011; Zhong et al.,
89 2017) and abnormal sea surface temperature (Li et al., 2019b; Wu et al., 2011). However, previous
90 studies on the cause of high temperature events usually only analyzed the correlation between
91 atmospheric circulation modes and the temperature indices along the time dimension, without
92 considering the spatial characteristics of the correlation.

93 From the above analysis, most of the researches mainly used the meteorological observation
94 temperature data interpolation to analyze local temperature changes, and as far as we know, no one
95 constructed continuous high-temporal resolution T_{\max} for high temperature analysis in China. In

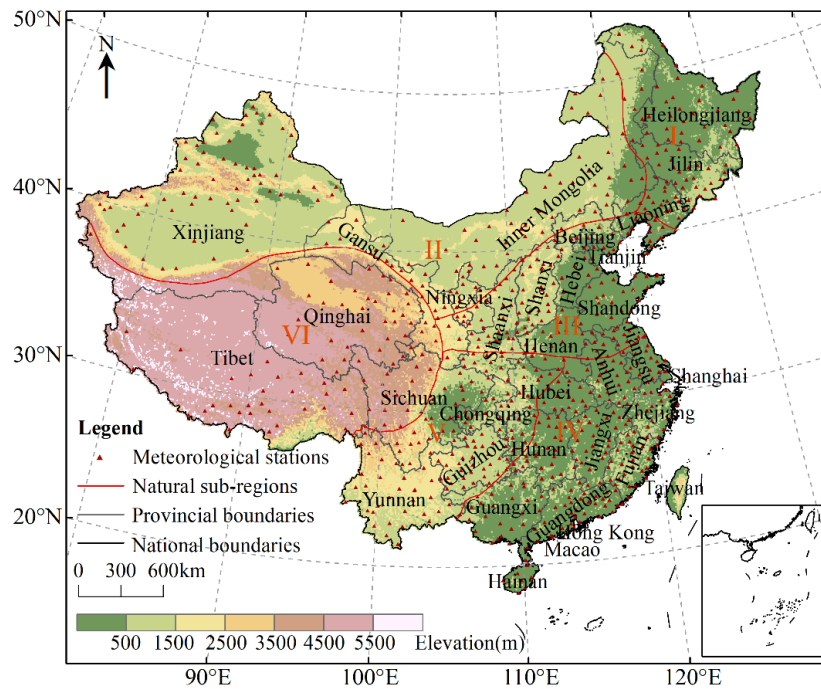
96 order to better study regional high temperature events, this study proposes an estimation framework
97 for obtaining high-precision T_{\max} . Firstly, we used multi-source data and established near surface T_a
98 diurnal variation model to build T_{\max} dataset in China from 1979 to 2018. To further improve the
99 accuracy, we divided China into six regions according to climate conditions and topography, and
100 established calibration models respectively. On this basis, we further analyzed the spatial-temporal
101 variation characteristics of T_{\max} and corresponding influencing factors in China. This can provide
102 evidence for mitigating global climate change and reducing regional carbon emissions for
103 environmental protection.

104 **2 Study area**

105 In order to establish a more high-precision T_{\max} dataset to analyze the temporal and spatial
106 characteristics of high-temperature in China, we divided China into six regions mainly based on
107 topographic conditions (elevation), and climatic conditions (T_a and precipitation), as shown in Fig.1.

108 (I) The northeast region has a temperate monsoon climate. Affected by the monsoon, T_a in the
109 southern part of the region is higher than that in the north in winter. The topography of this area is
110 dominated by plains, hills, and mountains. Due to the influence of topography, the variability of T_a
111 is large in local areas. (II) The northwestern region is dominated by a temperate continental climate
112 (cold in winter and hot in summer) with a large annual and daily T_a range. The area exhibits little
113 annual precipitation which decreases from east to west. The topography of this area is dominated
114 by plateau basins and rivers are scarce. (III) North China is located in a semi-humid and humid zone
115 in the warm temperate zone. Precipitation is mainly concentrated in summer. This area is dominated
116 by plains and plateaus, bounded by Taihang Mountain, the Loess Plateau in the west, and the North
117 China Plain in the east. (IV) The southeast region is dominated by mountains and hills, which

118 belongs to the warm and humid subtropical oceanic monsoon climate zone, and the tropical
 119 monsoon climate zone. The climate is mild, with an annual average T_a of 17-21°C and an average
 120 rainfall of 1400-2000mm. (V) The southwestern region has a subtropical monsoon climate, affected
 121 by the southeast monsoon and southwest monsoon. It is hot and rainy in summers, and the landforms
 122 in this area are dominated by plateaus and mountains. (VI) The Qinghai-Tibet Plateau is located in
 123 southwest China, with an average elevation of more than 4,000 meters. The towering terrain has a
 124 great impact on the climate in eastern and southwestern China. It has a plateau mountainous climate,
 125 with cold winters and warm summers, with aridity and little rain throughout the year.



126
 127 **Figure 1.** Overview of the study area.

128 **3 Data**

129 **3.1 China Meteorological Forcing Dataset (CMFD)**

130 CMFD is developed by the Hydro-meteorological Research Group of the Institute of Tibetan Plateau
 131 Research, Chinese Academy of Sciences. The dataset can be obtained from the National Qinghai-
 132 Tibet Plateau Science Data Center (<https://data.tpdc.ac.cn/>). The near surface T_a data of CMFD has

133 a time resolution of 3h and a spatial resolution of 0.1° , and its accuracy in China is better than Global
134 Land Data Assimilation System (GLDAS) data (He et al., 2020). CMFD data used ANUSPLIN
135 software to interpolate the difference between GLDAS T_a data and the measured T_a data to obtain
136 grid data, and then the difference grid data and the spatially downscaled GLDAS T_a data were
137 spatially added to generate high resolution T_a data. The T_a data of CMFD have been widely used in
138 climate simulation, hydrological simulation, vegetation greenness research, and cross-validation of
139 new T_a datasets (Luan et al., 2020; Gu et al., 2020; Wang et al., 2020). Although this dataset has
140 become one of the most widely used climate datasets in China, it does not provide the T_{max} value.
141 In order to perform high temperature analysis, we need to construct a T_{max} dataset.

142 3.2 ERA5 data

143 ERA5 data is the fifth generation of global climate reanalysis data produced by the European Centre
144 for Medium-range Weather Forecast (ECMWF) after ERA-Interim. The model version used by
145 ERA5 is IFS Cycle 41r2, and its spatial-temporal resolution and number of vertical layers are much
146 higher than the ERA-Interim data (Hoffmann et al., 2019; Urraca et al., 2018; Hersbach et al., 2020).
147 ERA5 reanalysis data provide a variety of meteorological elements, including atmospheric
148 parameters, land parameters, and ocean parameters, spanning a time range from 1950 to present.
149 The data can be obtained from Copernicus Climate Data Store (<https://cds.climate.copernicus.eu/>).
150 The ERA5 dataset also does not provide the T_{max} . This study used T_a data from 1979 to 2018 with
151 a time resolution of 1 h and a spatial resolution of 0.25° to help build a T_{max} estimation model to
152 generate T_{max} value, and we have performed multiple kinds of data assimilation.

153 3.3 Meteorological station data

154 T_{\max} data from the China Surface Climatic Data Daily Dataset (V3.0) from 1979 to 2018 were used
155 to verify the accuracy of T_{\max} estimations. The hourly T_a observation data from China
156 meteorological stations were used to determine the occurrence times of T_{\max} and daily lowest air
157 temperature (T_{\min}). Both datasets are from CMA National Meteorological Information Center
158 (<http://data.cma.cn/>). The data were subjected to preliminary quality control and evaluation by CMA,
159 and all elements in the observational data are of high quality and completeness, with the validity
160 rate generally above 99%. These datasets have been widely used in Chinese climate research (Li et
161 al., 2019a; Tong et al., 2019). To ensure the validity of the site data, manual checks were performed
162 on all observed data, including extreme value tests and spatial-temporal consistency tests, and
163 continuous missing data due to instrument damage and other reasons were eliminated. There are
164 824 stations for T_{\max} observation data and 2633 stations for hourly T_a observation data. After
165 performing checks and tests, we used T_{\max} data from 760 meteorological ground stations and hourly
166 T_a data from 2421 meteorological ground stations.

167 3.4 Ocean climate modal indices

168 The ocean occupies about 71% of the earth's surface area, which has a great impact on climate
169 change. After considering the distribution characteristics of China's land and sea, we analyzed the
170 effects of the following ocean climate modal indices on high temperature in China: Indian Ocean
171 Basin warming (IOBW) index, North Atlantic Oscillation (NAO) index, and NINO3.4 area sea
172 surface temperature (NINO3.4) index. Among them, the IOBW index comes from the National
173 Climate Center of CMA (<http://cmdp.ncc-cma.net/cn/index.htm>), and the NAO index and NINO3.4
174 index are from the National Oceanic and Atmospheric Administration of the United States

175 (<https://psl.noaa.gov/data/climateindices/list/>). The time range of the three indices is 1979-2018, and
176 the time scale is monthly.

177 **4 Methodology**

178 4.1 T_{\max} dataset construction

179 At present, the data used in the research on high temperature characteristics is mostly meteorological
180 station data, or grid data obtained by interpolation of station data. A limited number of stations
181 cannot represent the high temperature distribution at large scale. For regions where the stations are
182 very sparse, grid data obtained by spatial interpolation can hardly meet the accuracy requirements
183 of high temperature feature analysis. Although LST can be used to estimate T_{\max} , LST has degraded
184 value in the presence of clouds or rainfall. Therefore, in order to obtain a T_{\max} dataset with high
185 temporal and spatial resolution, we propose a T_{\max} construction model that combines meteorological
186 station data and reanalysis data, and consider the T_{\max} construction under clear sky and non-clear
187 sky conditions (see Section 4.1.1 for details). The data processing process is shown in Fig. 2, and
188 the data construction model is divided into two steps: T_{\max} estimation and T_{\max} correction. First, the
189 occurrence time of T_{\max} and T_{\min} was determined pixel by pixel (see Section 4.1.1 for details). Then,
190 T_{\max} was determined according to the weather state. (1) In clear sky conditions, CMFD 3h near-
191 surface T_a data was used to construct the T_a diurnal variation model which in turn yielded T_{\max} . (2)
192 In non-clear sky conditions, the site and reanalysis data were used to fill pixels. Finally, the
193 correction model was used to correct the poor quality pixels to generate the final T_{\max} dataset in
194 China.

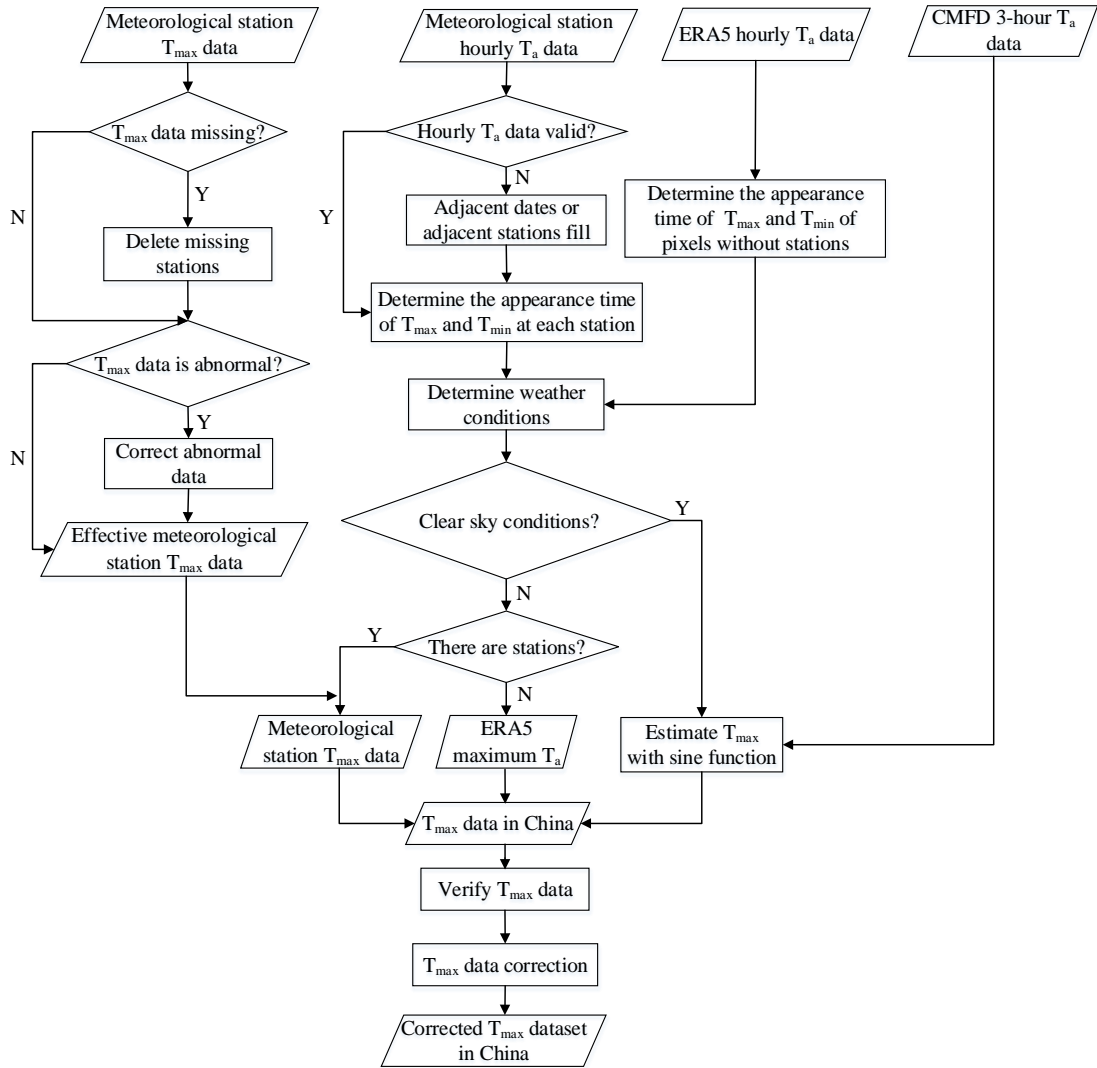


Figure 2. Technical roadmap for T_{\max} estimation.

4.1.1 T_{\max} estimation

The changes of T_a under different weather conditions are different. The changes of T_a under clear sky conditions are relatively smooth and regular. Under non-clear sky conditions, T_a changes more drastically. In order to improve the accuracy of T_{\max} estimation, we determined the occurrence time of T_{\max} and T_{\min} pixel by pixel. If there was a meteorological station at the pixel location, the analysis could be divided into two situations. (1) If hourly T_a data was valid, it was directly used to determine the occurrence time of T_{\max} and T_{\min} . (2) If there was a missing value in the hourly T_a data at a certain time, then we used the valid data from adjacent stations at the same time or adjacent time at the same stations to fill in the missing values. At present, there are not many meteorological stations in China, and the pixels without stations account for 97.5%. If there was no meteorological station at the pixel location, we used ERA5 hourly T_a data to determine the occurrence time of T_{\max} and

208 T_{\min} . Since the spatial resolution of the ERA5 data is lower than that of the dataset we produce, in
 209 order to match the two data spatially, we sample the two data to the same resolution, and then use
 210 latitude and longitude as control conditions to match the different data.

211 Studies have shown that the change of T_a under clear sky conditions follows a certain law: the
 212 change curve of T_a during the day is close to a sine function (Ephrath et al., 1996; Johnson and
 213 Fitzpatrick, 1977; Parton and Logan, 1981; Zhu et al., 2013), so we used sine function to simulate
 214 the change of T_a during the day. The appearance time of T_{\min} is t_{\min} , and the appearance time of
 215 T_{\max} is t_{\max} . According to the periodicity of the sine function, the model of the change of T_a during
 216 the day is obtained like Eq. (1).

$$217 \quad T_a(t) = A \sin\left(\frac{\pi(t-t_{\min})}{t_{\max}-t_{\min}} - \frac{\pi}{2}\right) + B \quad (1)$$

$$218 \quad \begin{cases} \frac{\partial \delta}{\partial A} = \sum_{i=1}^n \left\{ 2 * \sin\left(\frac{\pi(t_i-t_{\min})}{t_{\max}-t_{\min}} - \frac{\pi}{2}\right) * \left[A * \sin\left(\frac{\pi(t_i-t_{\min})}{t_{\max}-t_{\min}} - \frac{\pi}{2}\right) + B - T_{ai} \right] \right\} = 0 \\ \frac{\partial \delta}{\partial B} = \sum_{i=1}^n \left\{ 2 * \left[A * \sin\left(\frac{\pi(t_i-t_{\min})}{t_{\max}-t_{\min}} - \frac{\pi}{2}\right) + B - T_{ai} \right] \right\} = 0 \\ \delta = \sum_{i=1}^n \left[A * \sin\left(\frac{\pi(t_i-t_{\min})}{t_{\max}-t_{\min}} - \frac{\pi}{2}\right) + B - T_{ai} \right]^2 \end{cases} \quad (2)$$

219 Here n is the number of CMFD near surface T_a data used to construct the T_a change model in a
 220 day. CMFD can obtain T_a data 8 times a day. This study uses four daytime T_a data to construct a T_a
 221 variation model, so n is 4. T_{ai} is the near surface T_a data at the i th time of CMFD, and δ is the sum
 222 of squares of the difference between the model estimated T_a and the near surface T_a of the CMFD.
 223

224 Since the change of T_a under non-clear sky conditions does not conform to the sine curve change,
 225 we divided the estimation of T_{\max} under non-clear sky conditions into two situations. (1) If there
 226 was a station at the location of the pixel, the measured T_{\max} at the station was directly used as the
 227 T_{\max} of the pixel. (2) If there was no measured T_{\max} at the pixel location, the highest value of hourly
 228 T_a of ERA5 in a day was taken as T_{\max} . Then T_{\max} determined by the ERA5 data was assigned to
 229 the pixel at the corresponding position of the T_{\max} image we established using the spatial matching
 230 method.

231 4.1.2 T_{\max} correction

232 The validation of T_{\max} showed some differences between the estimated T_{\max} and the measured T_{\max} .
 233 In order to further improve the accuracy of T_{\max} , the measurements taken at weather stations should
 234 be used to correct the estimated T_{\max} , as shown in Fig. 3. First, determine whether there is station

235 data at the pixel location. For pixels with stations, it is further judged whether the estimated T_{\max} is
 236 valid by comparing the measured T_{\max} with the estimated T_{\max} . For a pixel with poor quality, if there
 237 is station data at the location of the pixel, the low-quality pixel will be replaced with the measured
 238 data from the station. If there is no station data at the pixel location, the data is corrected by multiple
 239 linear regression method (Ninyerola et al., 2000; Zhao et al., 2020; Zheng et al., 2013). By
 240 establishing the regression relationship between station T_{\max} and estimated T_{\max} , the residuals were
 241 calculated according to the measured values and T_{\max} regression predicted values, and the spatial
 242 distribution of the residuals was obtained by the inverse distance weight (IDW) interpolation method.
 243 Finally, the estimated T_{\max} and the residual were added to obtain the corrected T_{\max} . The calibration
 244 model is like Eq. (3) and Eq. (4).

$$245 \quad T_{after}(i, j) = T_{before}(i, j) + \hat{\epsilon}(i, j) \quad (3)$$

$$246 \quad \hat{\epsilon}(i, j) = T_{true}(i, j) - T_{forecast}(i, j) \quad (4)$$

247 Here i and j are the row and column numbers of the image, $T_{after}(i, j)$ is T_{\max} after correction,
 248 $T_{before}(i, j)$ is T_{\max} before correction, $\hat{\epsilon}(i, j)$ is the residual, $T_{true}(i, j)$ is the measured T_{\max} , and
 249 $T_{forecast}(i, j)$ is T_{\max} predicted by the regression model.

250 We used the jackknife method to randomly divide the station data into calibration and
 251 verification data (Benali et al., 2012; Zhao et al., 2020). We selected 80% of the meteorological
 252 stations to establish the regression relationship between the measured and estimated T_{\max} values.
 253 The other 20% of the meteorological stations were used to verify the accuracy of the corrected data.
 254 In order to improve data accuracy, the dataset used in the subsequent analysis of spatial-temporal
 255 variation of high temperature was the data corrected by all stations. Due to the different topographic
 256 and climatic characteristics of the six natural regions, the linear models of estimated T_{\max} and
 257 measured T_{\max} in each region were different. In order to obtain a higher-precision correction, the six
 258 regions were corrected separately.

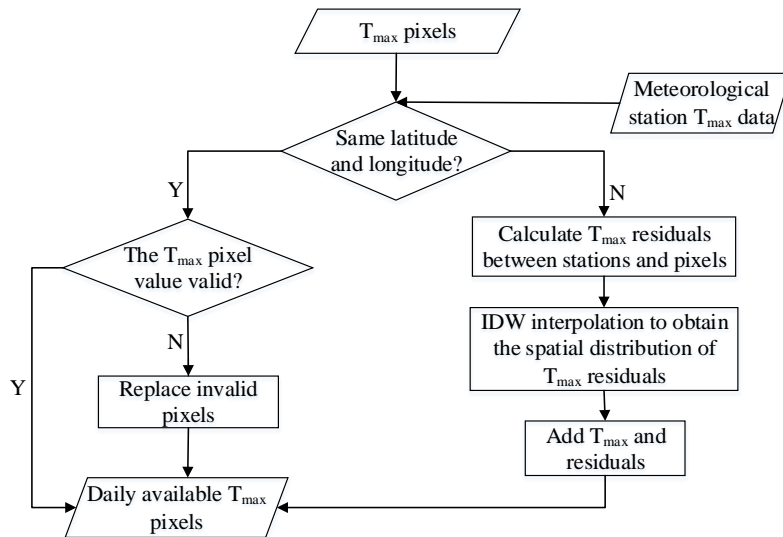


Figure 3. Flow chart of T_{\max} correction.

4.2 Extreme temperature indices

ETCCDI proposed a set of extreme climate indices in the Climate Change Monitoring conference, which became the unified standard for climate change research (Hong and Ying, 2018; Mcgree et al., 2019; Poudel et al., 2020; Zhang et al., 2019; Zhou et al., 2016). Among them, 27 indices are considered as core indices, which are calculated from daily T_a and precipitation data and have the characteristics of weak extremeness, low noise, and strong significance. These indices comprehensively capture the frequency, intensity and duration of extreme climate events, and are recommended as the core indicators for extreme climate event analysis by the STARDEX program of the European Union (Guan et al., 2015; Ruml et al., 2017). In this study, six temperature indices related to T_{\max} were used to analyze high temperature characteristics, and their definitions are shown in Table 1. Among them, the 90th percentile in TX90p and the 10th percentile in TX10p were obtained in ascending order based on the T_{\max} data of each month during 1979-2018.

Table 1. Definition of extreme temperature indices.

Index	Name	Definition	Category	Unit
SU	Summer days	Annual count of days when $T_{\max} > 25^{\circ}\text{C}$	Frequency	d
TX90p	Warm days	Annual count of days when $T_{\max} > 90\text{th}$ percentile	Frequency	d
TXn	Minimum T_{\max}	Annual minimum value of T_{\max}	Intensity	$^{\circ}\text{C}$
TXx	Maximum T_{\max}	Annual maximum value of T_{\max}	Intensity	$^{\circ}\text{C}$

ID	Icing days	Annual count of days when $T_{\max} < 0^{\circ}\text{C}$	Frequency	d
TX10p	Cold days	Annual count of days when $T_{\max} < 10\text{th percentile}$	Frequency	d

274 4.3 Trend analysis

275 4.3.1 Sen's slope estimation

276 In this study, the trends of T_{\max} and extreme temperature indices were calculated using Sen's slope
 277 estimation. Sen's slope estimation is a nonparametric estimation method. Even if there are some
 278 outliers in the sample, it can reliably estimate the change trend of the time series, so it is widely used
 279 in trend analysis (Sen, 1968; Zhang et al., 2017). The Eq. (5) is used to calculate the slope of each
 280 pair of data.

$$281 \quad K_i = \frac{x_k - x_j}{k - j} \quad (i = 1, 2, \dots, N) \quad (5)$$

282 Where $N = \frac{n(n-1)}{2}$, x_k and x_j are the time series values of the k th and j th samples respectively
 283 ($1 \leq j < k \leq n$). Arranging the N , K_i values in ascending order, the median Sen's slope is
 284 estimated as Eq. (6).

$$285 \quad \text{Slope} = \begin{cases} K_{[(N+1)/2]} & , N \text{ is odd} \\ \frac{K_{[N/2]} + K_{[(N+2)/2]}}{2} & , N \text{ is even} \end{cases} \quad (6)$$

286 4.3.2 Mann-Kendall trend test

287 Mann-Kendall trend test is used to test the trends of T_{\max} and extreme temperature indices. Mann-
 288 Kendall method does not require samples to follow a certain distribution and is not disturbed by a
 289 few outliers, and it can test the change trend of time series (Seenu and Jayakumar, 2021; Tan et al.,
 290 2019). Eq. (7) is used to calculate the statistic of the Mann-Kendall trend test.

$$291 \quad S = \sum_{i=1}^{n-1} \sum_{j=i+1}^n \text{sgn}(x_j - x_i) \quad (7)$$

$$292 \quad \text{sgn}(x_j - x_i) = \begin{cases} 1 & , x_j - x_i > 0 \\ 0 & , x_j - x_i = 0 \\ -1 & , x_j - x_i < 0 \end{cases} \quad (8)$$

$$293 \quad \text{Var}(S) = \frac{n(n-1)(2n+5)}{18} \quad (9)$$

294 Here x_i and x_j are the i th and j th data values of the time series, and n is the length of the time
 295 series, where n is 40. $\text{Var}(S)$ is the variance of S . The standardized statistic Z_c is computed by using
 296 Eq. (10).

$$Z_c = \begin{cases} \frac{S-1}{\sqrt{\text{Var}(S)}}, S > 0 \\ 0, S = 0 \\ \frac{S+1}{\sqrt{\text{Var}(S)}}, S < 0 \end{cases} \quad (10)$$

When $|Z_c| > Z_{1-\alpha/2}$, the change trend is considered to be significant. Here, $Z_{1-\alpha/2}$ is the standard normal variance, α is the significance test level, when $\alpha = 0.05$, $Z_{1-\alpha/2} = 1.96$, and when $\alpha = 0.01$, $Z_{1-\alpha/2} = 2.58$.

4.4 Mann-Kendall test for abrupt change analysis

Climate system change is an unstable and discontinuous change process, and one of the commonly used methods to test its change is the Mann-Kendall mutation test, which is very effective in testing the change of elements from a relatively stable state to another state (Ruml et al., 2017). We used Mann-Kendall mutation test to test whether extreme temperature indices has mutation. For a time series x with n samples, Eq. (11) is used to construct an ordered sequence.

$$s_k = \sum_{i=1}^k r_i \quad (k = 2, 3, \dots, n) \quad (11)$$

$$r_i = \begin{cases} +1, x_i > x_j \\ 0, x_i \leq x_j \end{cases} \quad (j = 1, 2, \dots, i) \quad (12)$$

$$UF_k = \frac{s_k - E(s_k)}{\sqrt{\text{Var}(s_k)}} \quad (k = 1, 2, \dots, n) \quad (13)$$

$$E(s_k) = \frac{k(k-1)}{4} \quad (14)$$

$$\text{Var}(s_k) = \frac{k(k-1)(2k+5)}{72} \quad (15)$$

Where s_k is the cumulative count of the number of values at time i greater than that at time j . $E(s_k)$ and $\text{Var}(s_k)$ are the mean and variance of the cumulative number s_k respectively. UF_k is a standard normal distribution, given the significance level α , and can be obtained from the normal distribution table. If $|UF_k| > U_\alpha$, which indicates that the variation trend of time series is significant. Reverse the time series x to x_n, x_{n-1}, \dots, x_1 , and repeat the above process with $UB_k = -UF_k (k = n, n-1, \dots, 1)$.

318 4.5 Correlation analysis

319 Pearson correlation coefficient is often used to accurately measure the degree of correlation between
320 two variables, and its size can reflect the strength of the correlation of the variables. For
321 variables x_1, x_2, \dots, x_n and variables y_1, y_2, \dots, y_n , the correlation coefficient between them is
322 calculated as Eq. (16).

$$323 \quad R = \frac{n \sum_{i=1}^n (x_i \times y_i) - \sum_{i=1}^n x_i \sum_{i=1}^n y_i}{\sqrt{n \sum_{i=1}^n x_i^2 - (\sum_{i=1}^n x_i)^2} \sqrt{n \sum_{i=1}^n y_i^2 - (\sum_{i=1}^n y_i)^2}} \quad (16)$$

324 Here n is the total length of the time series. The value of R is between -1 and 1. $R < 0$ indicates a
325 negative correlation. $R > 0$ indicates a positive correlation. The closer the absolute value of R is to 1,
326 the closer the relationship between the two elements is.

327 5 Results

328 5.1 Validation

329 In order to verify the feasibility of T_{\max} estimation using the T_a diurnal variation model and to
330 analyze the accuracy of T_{\max} estimation in different regions, scatter plots of estimated T_{\max} and
331 measured T_{\max} in six natural regions (I, II, III, IV, V and VI) were drawn according to the regional
332 division in Fig. 1. The results are shown in Fig. 4, and the validation in each region shows that the
333 root mean square errors (RMSE) is between 2.38-2.94°C, and the mean absolute error (MAE) is
334 between 1.88-2.45°C, and the coefficient of determination (R^2) is between 0.95-0.99. In six regions,
335 the accuracy in region IV is the highest, while the accuracy is the lowest in region VI. As can be
336 seen from Fig. 4, although most of the data is very accurate, some have some room for improvement.
337 Therefore, further correction is needed to improve the accuracy of the T_{\max} dataset.

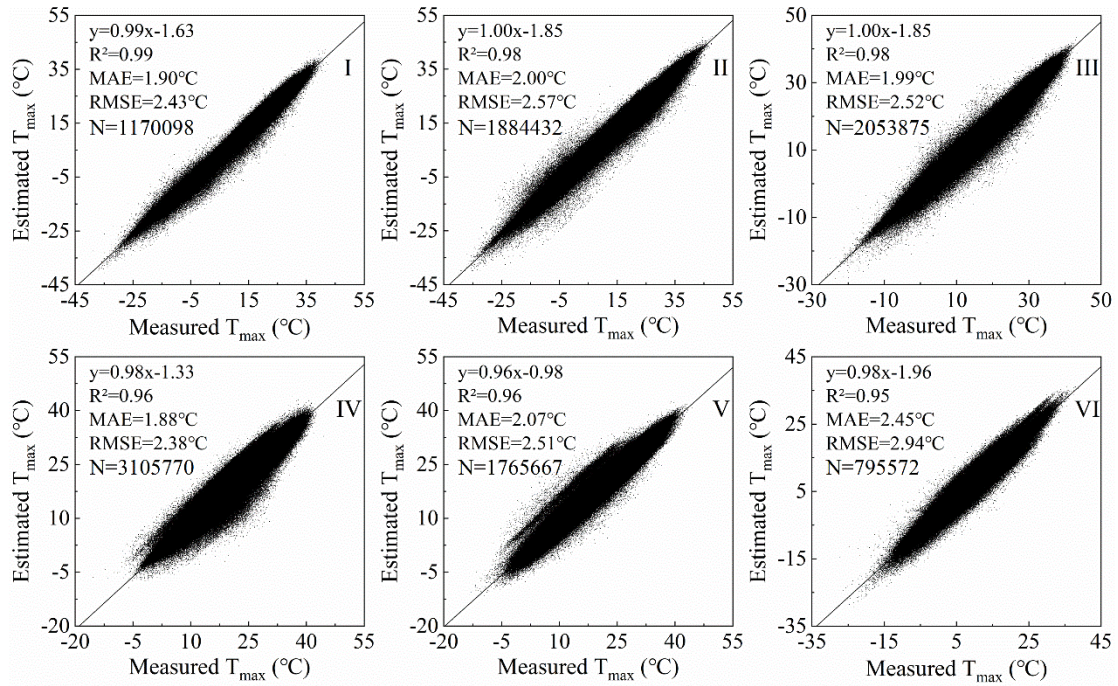


Figure 4. Validation of T_{\max} estimation results in each region.

338
 339
 340 The correction method in Sect. 4.1.2 was used to correct the T_{\max} estimation results of six regions
 341 separately. The comparison between T_{\max} before and after correction with the measured T_{\max} is
 342 shown in Fig. 5. It can be seen that T_{\max} corrected by the regression model is more consistent with
 343 the measured T_{\max} . The RMSE decreases from 2.38-2.94°C to 1.14-1.81°C, and the MAE decreases
 344 from 1.88-2.45°C to 0.84-1.38°C, and the R^2 increases from 0.96-0.99 to 0.97-0.99. The accuracy
 345 of T_{\max} is improved in each region after correction. The number of meteorological stations in region
 346 I is denser, and the accuracy of T_{\max} after calibration is significantly improved. The RMSE reduced
 347 from 2.32°C to 1.14°C, and the error is reduced by 51%. The number of meteorological stations in
 348 region VI is small, and the topography is undulating and the spatial heterogeneity is large. Therefore,
 349 the accuracy in this region is still the lowest among the six natural areas after correction. In general,
 350 the corrected T_{\max} dataset has higher consistency with the measured data, and which can be applied
 351 to research related to regional scale T_{\max} .

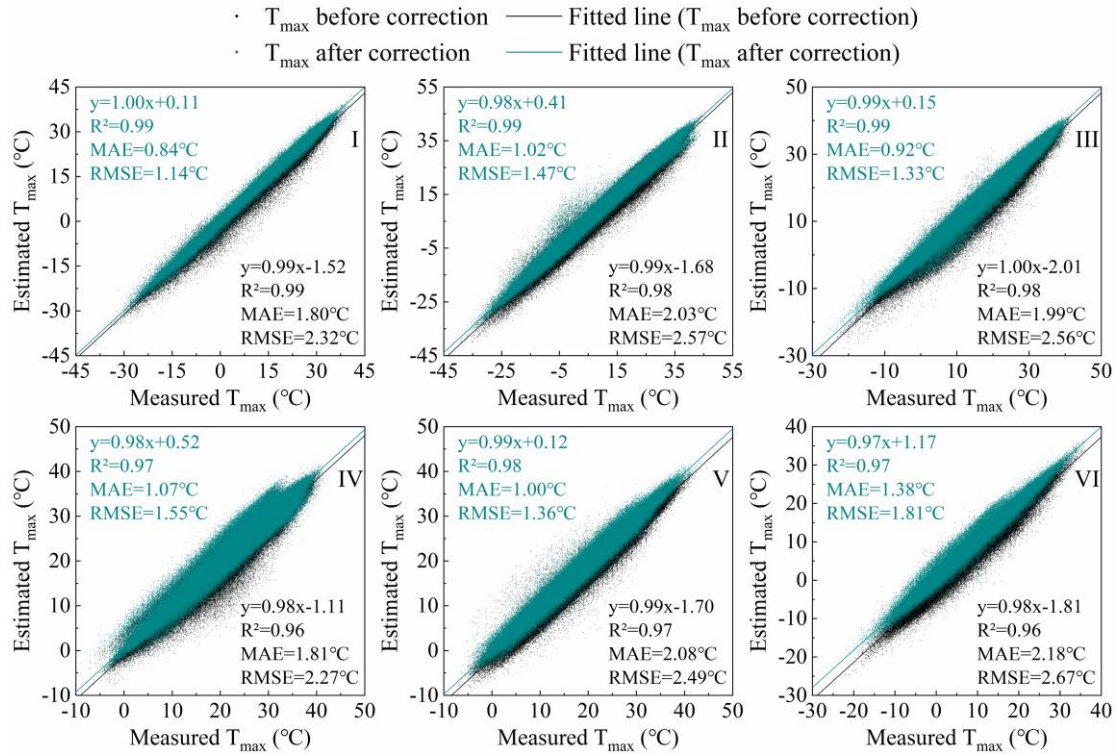


Figure 5. Validation of T_{\max} after correction.

5.2 Temporal and spatial changes of T_{\max}

5.2.1 Inter-annual variability

Fig. 6 shows the annual average change of T_{\max} in each region of China during 1979-2018. The T_{\max} in each region exhibited an upward trend. However, due to the different geographical locations and the influence of atmospheric circulation in various regions, the change of T_{\max} was also different.

The order of the T_{\max} increase in each region was: V>IV>III>Whole>VI>II>I. The T_{\max} anomaly

ranges of region I-VI and the whole China region were -1.41-1.53, -1.54-1.16, -1.47-1.12, -1.34-

0.92, -0.97-1.33, -1.31-1.15, and -1.09-0.98°C, respectively. The T_{\max} variation coefficients were

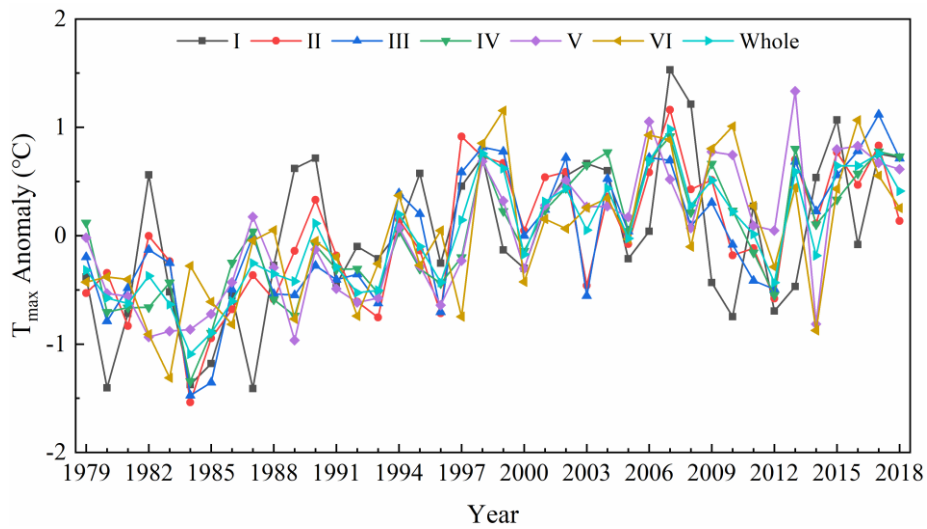
0.082, 0.045, 0.036, 0.024, 0.03, 0.088 and 0.038, respectively. It can be seen that T_{\max} fluctuated

the most in region VI and the least in region IV. The minimum values of region I-VI and China

region appeared in 1987, 1984, 1984, 1984, 1989, 1983, and 1984, respectively which were

distributed in the 1980s. The highest values of T_{\max} appeared in 2007, 2007, 2017, 2007, 2013, 1999,

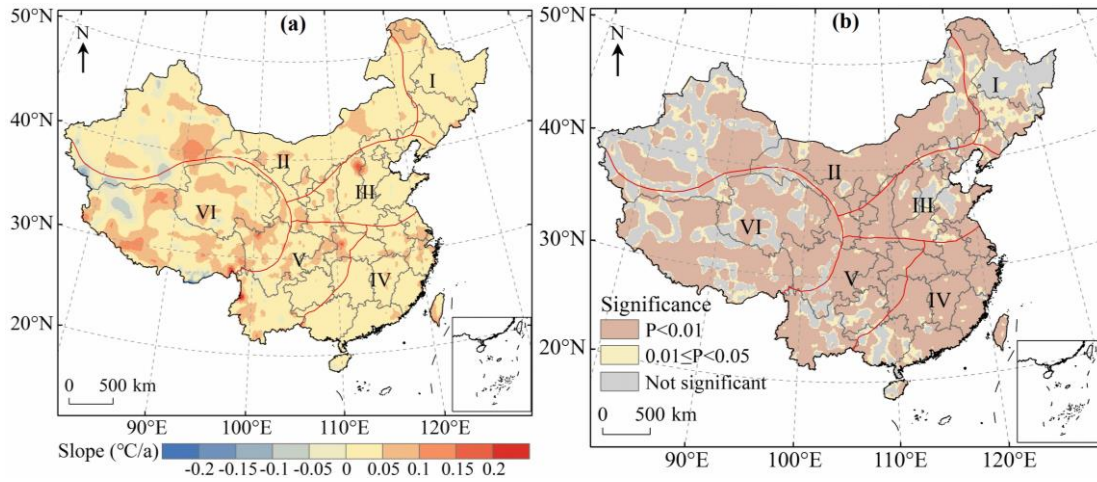
366 and 2007 respectively. Zhai et al. (2016) found that 1999, 2007, and 2013 were among the 10 years
 367 with the highest average T_a in China from 1900 to 2015. From 1998 to 2012, global surface
 368 temperature experienced a warming hiatus (Du et al., 2019; Li et al., 2015), and T_{max} in all regions
 369 of China showed a downward trend during this period.



370
 371 **Figure 6.** Inter-annual changes of T_{max} anomalies in six regions of China during 1979-2018.

372 In order to understand the spatial pattern and regional differences of T_{max} changes with more
 373 detail in China, Sen's slope estimation was used to calculate the annual average T_{max} change rate
 374 from 1979 to 2018 at the pixel scale (Fig. 7a). The significance test of the T_{max} change trend was
 375 conducted by the Mann-Kendall trend test (Fig. 7b). At the same time, the average change rate of
 376 T_{max} in each region and the area percentage of significant increase and decrease ($P<0.05$) of T_{max}
 377 were calculated (Table 2). The results indicated that the annual average T_{max} change rate in most
 378 regions of China (78.24% of the study area) passed the significance test with a confidence of 0.05,
 379 and 65.84% of the pixels showed very significant changes in T_{max} ($P<0.01$). Fig. 7a showed that the
 380 annual average T_{max} in most regions of China was on the rise, and the fastest rising rate of T_{max} was
 381 in western Yunnan. Only 8.13% of the regions in China showed a downward trend in T_{max} . These
 382 were concentrated mainly in the north and south of Xinjiang, and the northwest and south of Tibet.

383 Among the six regions, the average T_{\max} change rate of region V was the largest ($0.38^{\circ}\text{C}/10\text{a}$), and
 384 the average T_{\max} change rate of region I and region II was the lowest ($0.31^{\circ}\text{C}/10\text{a}$) (Table 2).



385

386

Figure 7. Inter-annual change rate of T_{\max} (a) and results of Mann-Kendall trend test (b).

387

Table 2. Statistics of T_{\max} change trends in various regions of China from 1979 to 2018.

Region	I	II	III	IV	V	VI	Whole
Mean ($^{\circ}\text{C}/10\text{a}$)	0.31	0.31	0.33	0.35	0.38	0.33	0.33
Significant upward (%)	65.21	69.45	87.03	92.29	87.00	67.93	75.13
Significant downward (%)	0.09	3.14	0	0.32	0.75	7.92	3.11

388

5.2.2 Seasonal changes

389

On the basis of the annual analysis, we also analyzed the seasonal changes. The seasons are divided

390

according to the months (spring from March to May, summer from June to August, autumn from

391

September to November, and winter from December to February). We plotted the seasonal variation

392

curve of T_{\max} in China from 1979 to 2018 (Fig. 8), and some information on the trend of T_{\max}

393

changes is shown in Table 3. The results indicated that T_{\max} in each region fluctuated the most in

394

winter and the least in summer. The highest T_{\max} in each region in spring, summer, autumn and

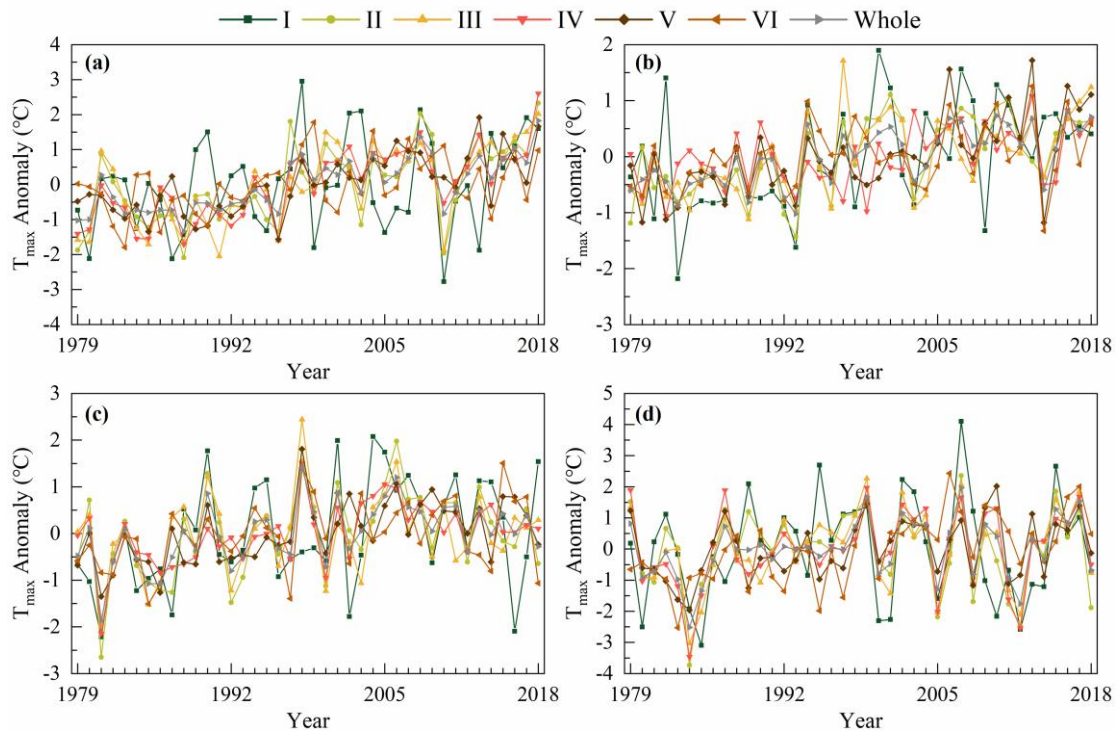
395

winter mostly occurred in 2018, 2013, 1998 and 2007, while the minimum T_{\max} in each region in

396

spring, summer, autumn and winter mostly occurred in 1988, 1993, 1981 and 1984. In 2013, T_{\max}

397 of region IV-VI in summer reached the highest since 1979, mainly due to the influence of the
 398 southwest monsoon, East Asian summer monsoon and other factors. Under the influence of El Niño,
 399 T_{\max} in winter in region I, II and the whole study area was the highest in 2007. Under the influence
 400 of La Niña, the minimum T_{\max} in spring and winter in most areas of China appeared in 1988 and
 401 1984, respectively. In the same season, the variation trend of T_{\max} in each region was significantly
 402 different, and some even had opposite trends. However, influenced by La Niña and the Eurasian
 403 atmospheric circulation, T_{\max} in winter in each region showed a consistent decreasing trend from
 404 2007 to 2008. As can be seen from Table 3, in spring, summer, autumn and winter, the regions with
 405 the fastest T_{\max} rise are III, I, I and VI respectively, and the regions with the lowest T_{\max} change rate
 406 are VI, VI, III and II respectively.



407
 408 **Figure 8.** Changes of T_{\max} anomalies in various regions of China in spring (a), summer (b), autumn (c), winter (d)
 409 during 1979-2018.

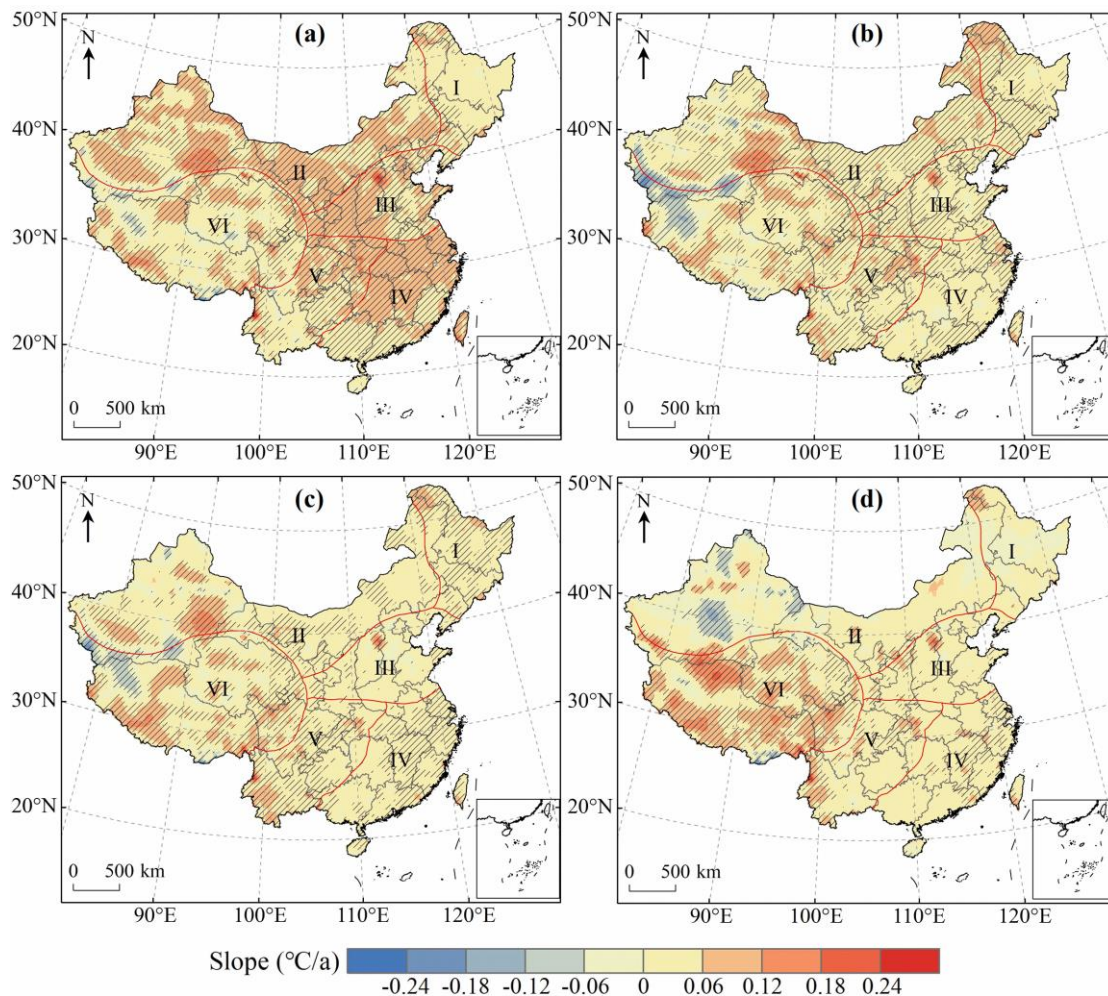
410 **Table 3.** Seasonal variation trend of T_{\max} in various regions of China from 1979 to 2018.

I	II	III	IV	V	VI	Whole
---	----	-----	----	---	----	-------

Spring	0.035	0.063**	0.072**	0.063**	0.051**	0.026*	0.048**
Summer	0.040**	0.035**	0.033**	0.022**	0.039**	0.020*	0.031**
Autumn	0.039*	0.024	0.014	0.025**	0.035**	0.025*	0.023**
Winter	0.009	-0.002	0.027	0.037	0.034*	0.058**	0.027

411 (*, ** represent the trends are significant at the level of $p=0.05$, $p=0.01$, respectively.)

412 In order to display the seasonal variation characteristics of T_{\max} in China more intuitively, we
413 drew the spatial distribution of the trend of T_{\max} and conducted a significance test (Fig. 9).
414 Meanwhile, we counted the percentage of significant increase and decrease of T_{\max} in each region
415 (Table 4). The results indicated that the areas with increasing T_{\max} were more than those with
416 decreasing T_{\max} in all seasons. From 1979 to 2018, the increasing trend of T_{\max} was most significant
417 in spring, which accounted for 92.73% of the total study area, followed by autumn and summer,
418 while T_{\max} increased the least in winter. Specifically, T_{\max} increased significantly in most parts of
419 China in spring, and the region where T_{\max} decreased significantly were mainly concentrated in the
420 region VI (Fig. 9a). In summer, T_{\max} in most part of China showed a significant increasing trend,
421 but T_{\max} in southern Xinjiang and northwestern Tibet exhibited a decreasing trend (Fig. 9b).
422 Compared with spring and summer, the area with a significant increasing trend of T_{\max} in autumn
423 was smaller, and the regions with a significant decreasing trend of T_{\max} were mainly distributed in
424 Xinjiang and Tibet (Fig. 9c). 79.02% of the regions experienced an increase in T_{\max} in winter, which
425 was significantly lower than in other seasons. A significant increasing trend of T_{\max} was observed
426 in the east of region IV, the southwest of regions V and VI, while the areas where T_{\max} decreased
427 significantly were mainly observed in Xinjiang (Fig. 9d). We also observed no significant decrease
428 in T_{\max} in regions I and III in spring, I in summer, I and IV in autumn, and III in winter (Table 4).
429 Further statistics showed that T_{\max} of the whole region III showed an upward trend in spring.



430

431

Figure 9. Spatial distribution of the change trend of T_{\max} in spring (a), summer (b), autumn (c), winter (d) over

432

China during 1979-2018. The shaded areas indicate trends that are significant at the 0.05 level.

433

Table 4. Change trend statistics of T_{\max} in different seasons over China from 1979 to 2018.

	Significant upward (%)				Significant downward (%)			
	Spring	Summer	Autumn	Winter	Spring	Summer	Autumn	Winter
I	35.12	74.75	65.75	6.89	0	0	0	0.10
II	81.56	73.47	36.07	8.10	1.01	7.04	3.15	10.87
III	97.71	69.05	14.67	15.99	0	0.38	0.06	0
IV	96.20	46.80	57.26	29.47	0.35	0.68	0	0.44
V	76.48	75.11	58.56	31.62	1.24	1.53	0.06	0.12
VI	50.20	55.11	49.54	68.58	7.00	14.17	10.34	2.28
Whole	71.46	65.39	45.86	29.40	2.29	6.04	3.61	4.01

434

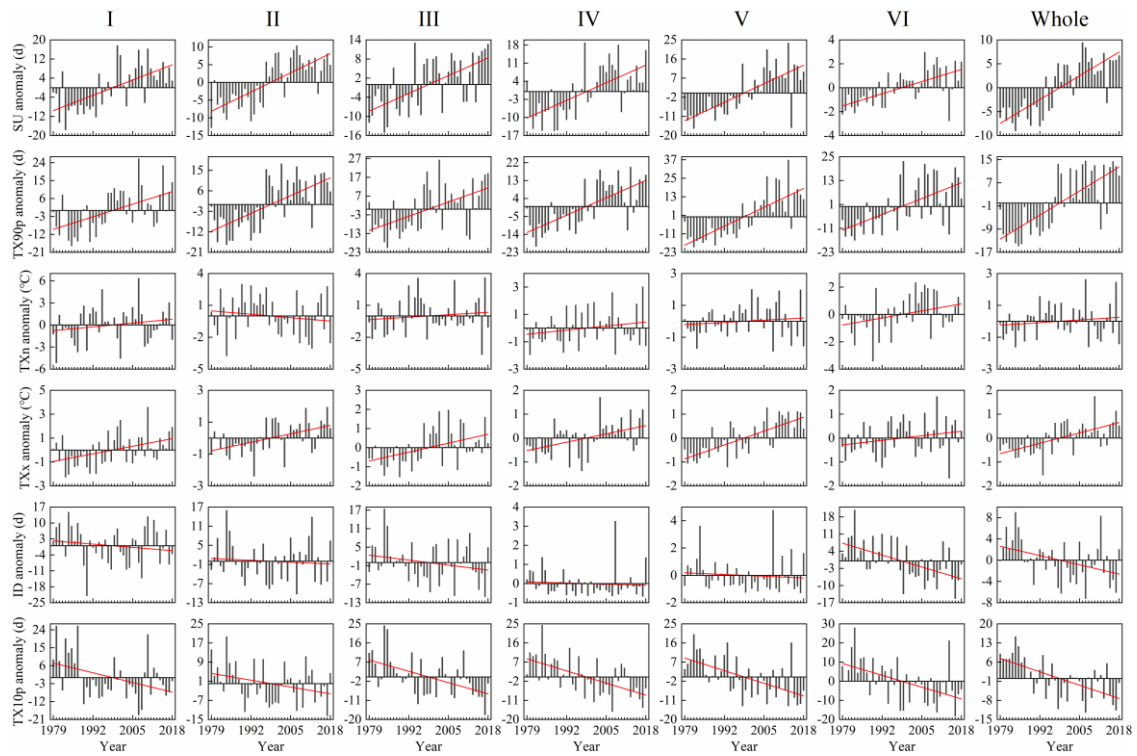
5.3 Temporal and spatial changes of extreme temperature indices

435

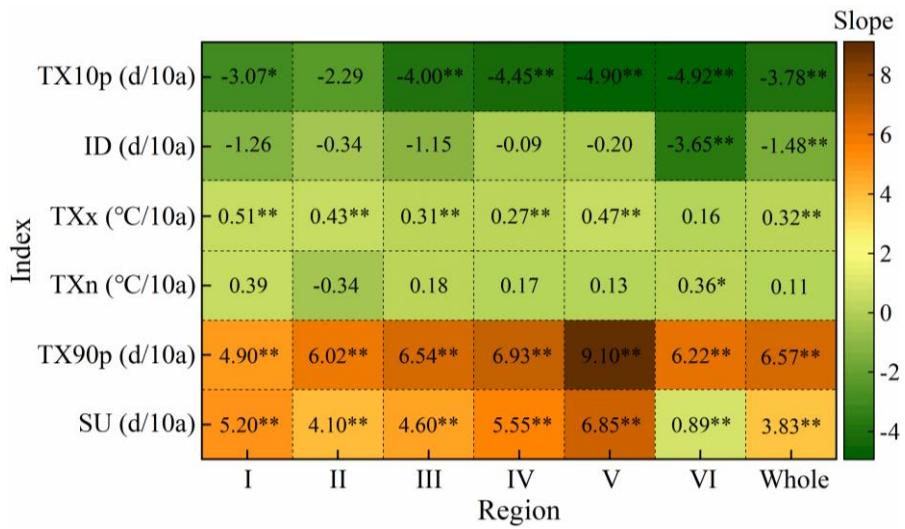
5.3.1 Change of time

436 We plotted the inter-annual variation of extreme temperature indices anomalies in various regions
437 of China from 1979 to 2018 (Fig. 10), and used Sen's slope estimation and the Mann-Kendall trend
438 test to calculate statistics on the trend of extreme temperature indices (Fig. 11). The results indicated
439 that SU, TX90p, TXn and TXx increased at a rate of 3.83d/10a, 6.57d/10a, 0.11°C/10a and
440 0.32°C/10a, respectively (Fig. 11). Influenced by the strong El Niño in 1997, the SU in all regions
441 exhibited a consistent upward trend from 1996 to 1997 (Fig. 10). The change rate of SU in all regions
442 passed the significance test of 0.01, indicating a significant upward trend (Fig. 11). The increasing
443 trend of TX90p in all regions was also very significant. The decadal average of TX90p in region
444 III-VI and the whole study area had an increasing trend, while the decadal average of TX90p in
445 region I and region II increased first and then decreased slightly. The TXn of region II showed a
446 weak decreasing trend, and the sliding average of the 3-year and 5-year periods also exhibited a
447 weak fluctuation downward trend. TXn of other regions showed an upward trend in general, and
448 only region VI had a significant increasing trend ($P < 0.05$) (Fig. 11). Except for region VI, the
449 change rate of TXx in other regions was higher than that of TXn. The rate of change of TXx
450 exhibited that the upward trend of region VI was not significant, while all other regions passed the
451 significance test of 0.01. During 1979-2018, ID and TX10p decreased significantly at the rate of -
452 1.48d/10a and -3.78d /10a, respectively ($P < 0.01$) (Fig. 11). The ID of all regions exhibited a
453 downward trend, with region VI and the whole study area showing the most obvious decline, passing
454 the significance test of 0.01 (Fig. 11). Compared with ID, TX10p decreased more sharply, and the
455 highest value of TX10p in all regions occurred before 1988 (Fig. 10). The above results indicate
456 that the frequency of high temperature events in China is on the rise, which is in line with the
457 expected results of global change. In addition, we also found that the occurrence time of maximum

458 and minimum values of SU, TXn, TXx and ID during 1979-2018 was consistent with previous
 459 research results by Hong and Ying (2018), which further proved the correctness of the T_{max} dataset
 460 constructed by us, indicating that the dataset can be used to analyze the spatial-temporal changes of
 461 high temperature in China.

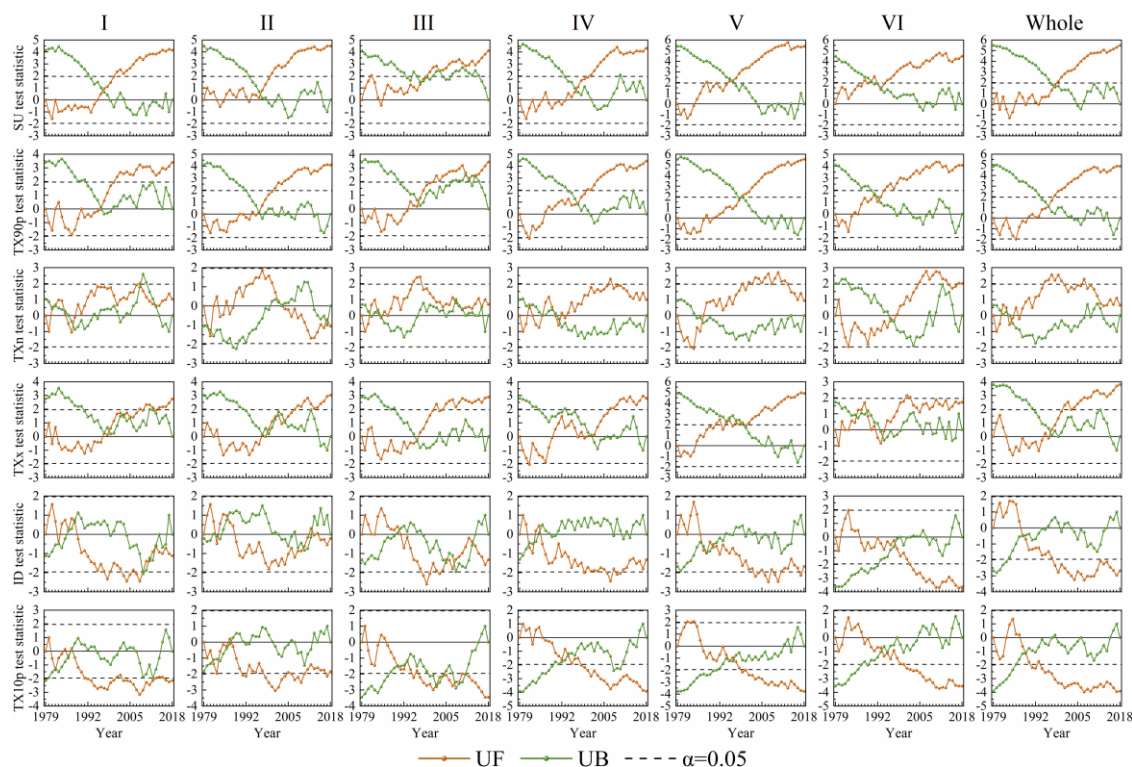


462
 463 **Figure 10.** Inter-annual trend of extreme temperature indices anomalies in different regions of China during 1979-
 464 2018.



465
 466 **Figure 11.** Variation trend of extreme temperature indices in different regions of China from 1979 to 2018. (*
 467 significant at the 0.05 level, ** significant at the 0.01 level.)

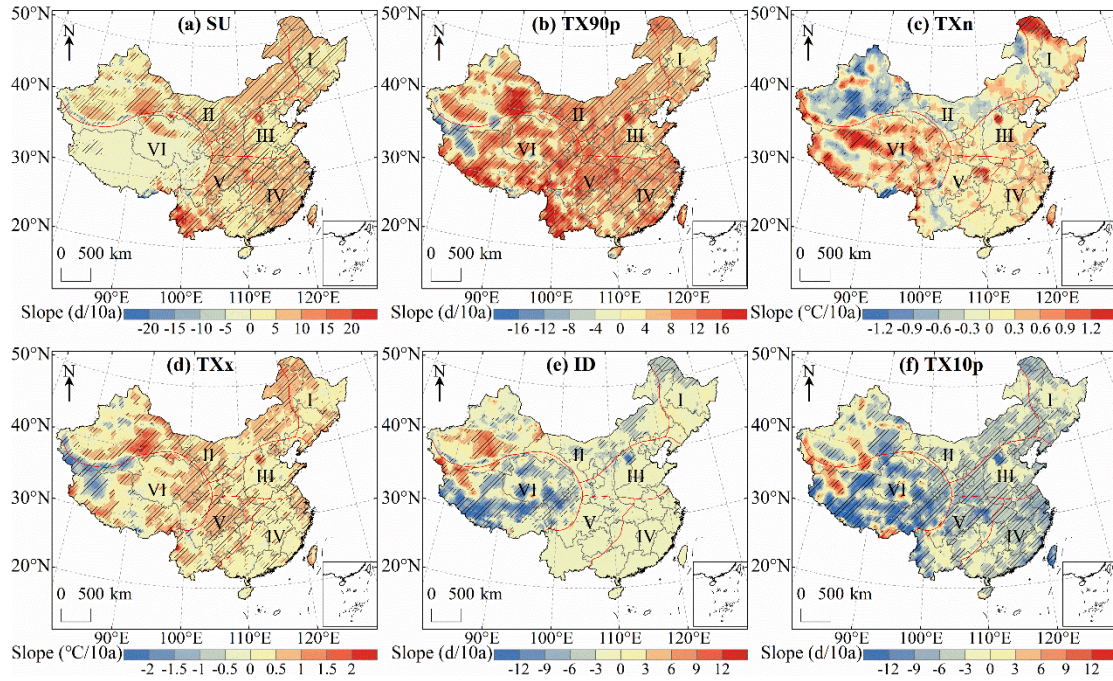
468 In order to analyze the variation rules of extreme temperature indices in China from 1979 to
 469 2018, the Mann-Kendall mutation test was applied to test the mutation characteristics of six extreme
 470 temperature indices at the significance level of 0.05. The results are shown in Fig. 12. We found
 471 that all the extreme temperature indices had abrupt change from 1979 to 2018, and 40% of the years
 472 where the abrupt changes occurred were El Niño years, while 46.7% were La Niña years. This
 473 finding further confirms that China is greatly affected by global climate change. TX90p in region I-
 474 II and the whole study area displayed an abrupt change from a period with lower value to one with
 475 higher value in 1996. After mutation in region II in 2003, TXn turned from an upward trend to a
 476 downward trend, but the downward trend was not obvious. The ID of the whole study area and its
 477 six sub-regions tended to increase first and then decrease.



478
 479 **Figure 12.** MK abrupt change detection for the extreme temperature indices in different regions of China during
 480 1979-2018.

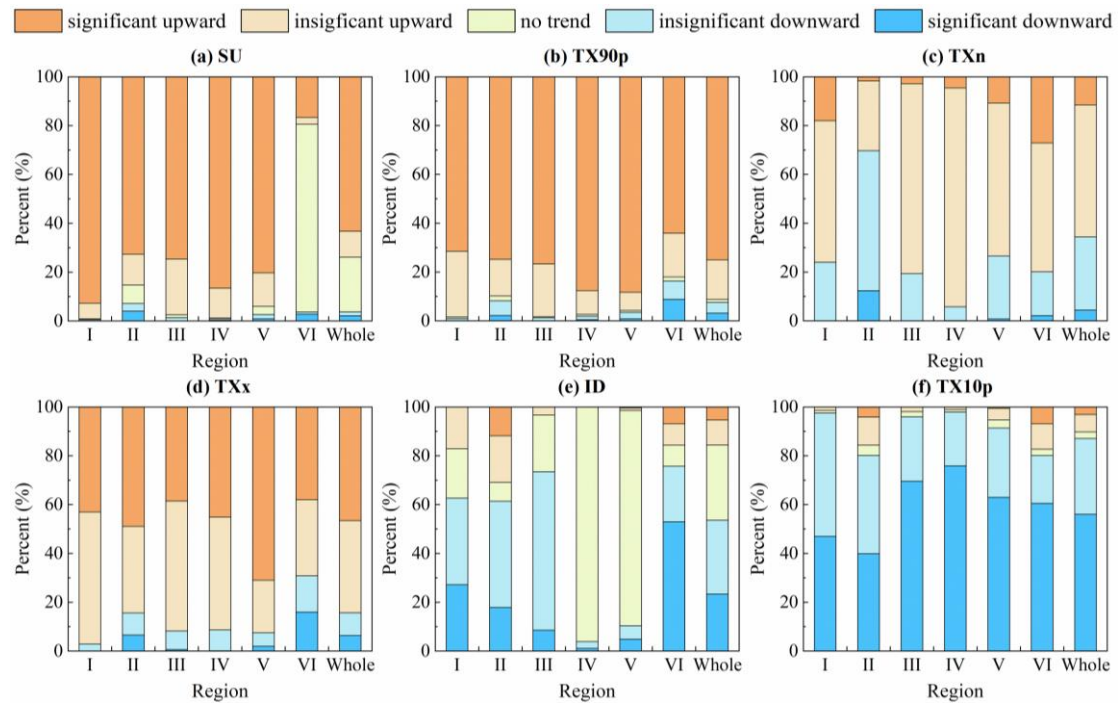
481 5.3.2 Spatial change

482 The spatial distribution of the extreme temperature indices trends in China during 1979-2018 is
483 shown in Fig. 13 (a-f), while the area percentage of the increasing and decreasing trend of extreme
484 temperature indices in each region is shown in Fig. 14 (a-f). For SU, TX90p, TXn and TXx, the area
485 with rising trend is larger than the area with declining trend. The change of SU in most regions of
486 China passed the significance test of 0.05, and the areas with significant increase accounted for 63.3%
487 of the whole study area (Fig. 14a). The regions with no significant change in SU were mainly
488 distributed in region VI (Fig. 13a). There were few days in a year when T_{\max} exceeded 25°C in
489 region VI, and T_{\max} in some regions was even lower than 25°C throughout the year, so the change
490 range of SU was small. The areas with a downward trend of TX90p were mainly distributed in
491 southern Xinjiang and northern Tibet (Fig. 13b). TX90p increased significantly in 75% of regions
492 in China ($P < 0.05$), and the area percentage of TX90p significantly increased in region V was the
493 largest among the six regions (Fig. 14b). The trend of TXn change in most regions of China was not
494 significant, and the significant decrease was mainly concentrated in region II and region VI (Fig.
495 13c). While other regions were dominated by increasing trend of the TXn, 69.7% of regions in
496 region II showed a downward trend (Fig. 14c). For TXx, its upward trend was slightly stronger than
497 TXn, and the region with the highest change rate was located in western China (Fig. 13d). The
498 regions with significantly decreased ID were mainly distributed in region VI (Fig. 13e). 75.7% of
499 the regions had a declining ID, and 53% of the regions passed the significance test (Fig. 14e). As
500 far as TX10p is concerned, its cooling trend was much stronger than that of ID, and the areas of
501 significant decline were widely distributed through all regions of China (Fig. 13f). The area with a
502 significant decrease in region IV accounted for 75.9% of the region, which was the largest among
503 the six regions (Fig. 14f).



504
505
506

Figure 13. Spatial distribution of trends in extreme temperature indices over China during 1979-2018. The shaded areas indicate trends that are significant at the 0.05 level.



507
508
509

Figure 14. Area percentage of the trend of extreme temperature indices in different regions of China during 1979-2018

510 **6 Discussion**

511 6.1 The influence of ocean climate modalities on T_{max}

512 The correlation between T_{max} anomalies and three climate modal indices in China during 1979-2018
513 is shown in Fig. 15 (a-c). The results show that there is a significant positive correlation between
514 T_{max} and IOBW in 54.18% of the regions in China, which indicates that the warming of the Indian
515 Ocean will contribute to the warming trend of T_{max} in these regions. T_{max} had a moderate positive
516 correlation ($0.4 < R < 0.6$, $P < 0.01$) with IOBW in southern Yunnan and eastern Hainan (Fig. 15a).
517 T_{max} and NAO had a significant positive correlation in northeast China, but the correlation was very
518 weak ($R < 0.2$). The percentage of T_{max} anomaly value negatively correlated with NAO (16.55%)
519 was higher than that of NAO positively correlated (5.27%), mainly distributed in the west and south
520 of region II, west of region III, south of region IV and V, and northeast of region VI. This indicated
521 that the positive phase of NAO contribute to the decrease of T_{max} in these regions (Fig. 15b). T_{max}
522 was significantly positively correlated with NINO3.4 in southern China, central Xinjiang and
523 southern Gansu, indicating that El Niño events will lead to higher temperatures in these regions. In
524 western China and the middle part of region IV, T_{max} was significantly negatively correlated with
525 NINO3.4, indicating that El Niño events will lead to cooling phenomena in these regions (Fig. 15c).

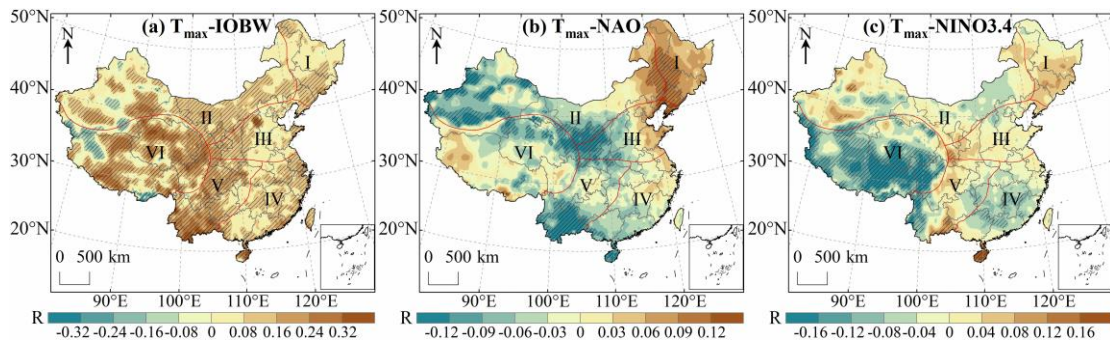
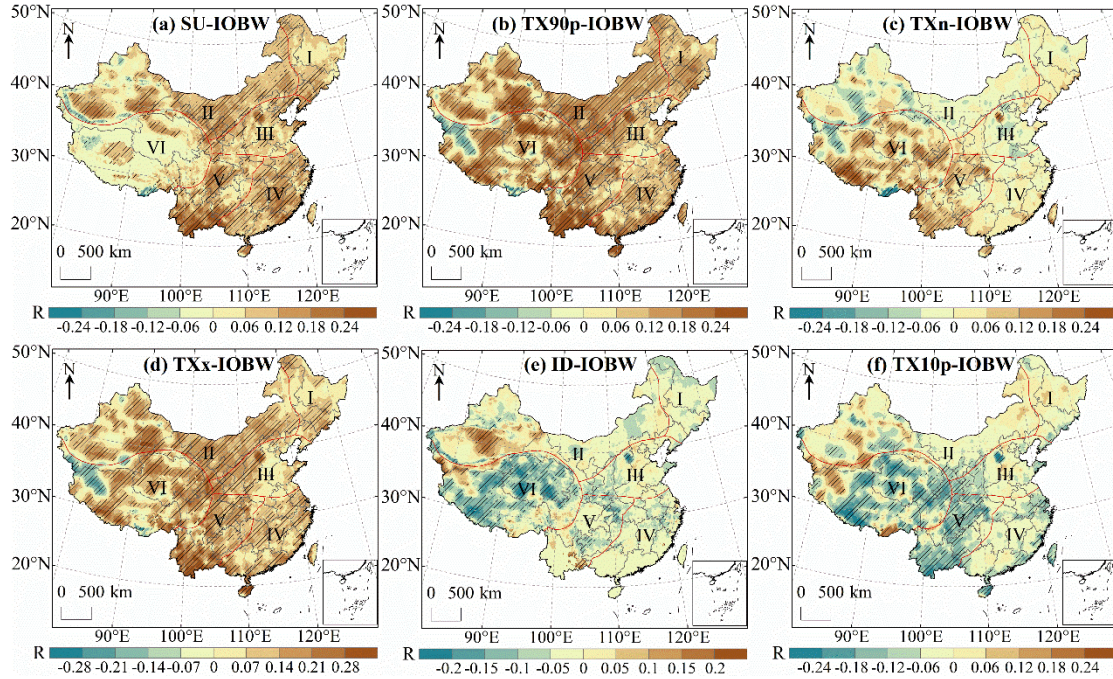


Figure 15. Correlation analysis between T_{max} and IOBW (a), NAO (b) and NINO3.4 (c) in China during 1979-

528 2018. The shaded areas indicate correlations that are significant at the 0.05 level.

529 6.2 The influence of ocean climate mode on extreme temperature indices

530 Fig. 16 (a-f) indicates the spatial distribution of the correlation between extreme temperature indices
531 anomalies and IOBW in China during 1979-2018. It can be seen that SU, TX90p, TXn and TXx
532 over most of China are positively correlated with the IOBW. The region with significant positive
533 correlation between the SU and IOBW accounted for 42.67% of the whole study area, which
534 indicated that a warming Indian Ocean would lead to the number of days over 25°C in these regions
535 to increase. Significant negative correlations were found in northwest and southeast Tibet and the
536 mountainous regions of southern Xinjiang (Fig. 16a). The area with the largest correlation
537 coefficient is in the northeast of Hainan ($R=0.48$). The significant negative correlation between
538 TX90p and IOBW was mainly distributed in region VI, but the negative correlation was not strong
539 ($|R| < 0.4$) (Fig. 16b). The correlation coefficient between TXn and IOBW ranged from -0.34 to
540 0.34, and the regions with significant positive correlation accounted for 16.65% of the whole study
541 area. TXn and IOBW were significantly negatively correlated mainly in western China (Fig. 16c).
542 Compared with TXn, the regions with significant correlation between TXx and IOBW were more
543 widely distributed in China, among which the correlation coefficients in southern Yunnan and
544 eastern Hainan were moderately positive ($0.4 < R < 0.6$) (Fig. 16d). ID and TX10p were negatively
545 correlated with IOBW in most of China. The regions with significant negative correlation between
546 ID and IOBW were mainly distributed in region VI, and the regions with significant positive
547 correlation were mainly distributed in the west of region II (Fig. 16e). TX10p has a significant
548 negative correlation with IOBW in more areas than ID, and the significant positive correlation was
549 mainly located in western China (Fig. 16f).

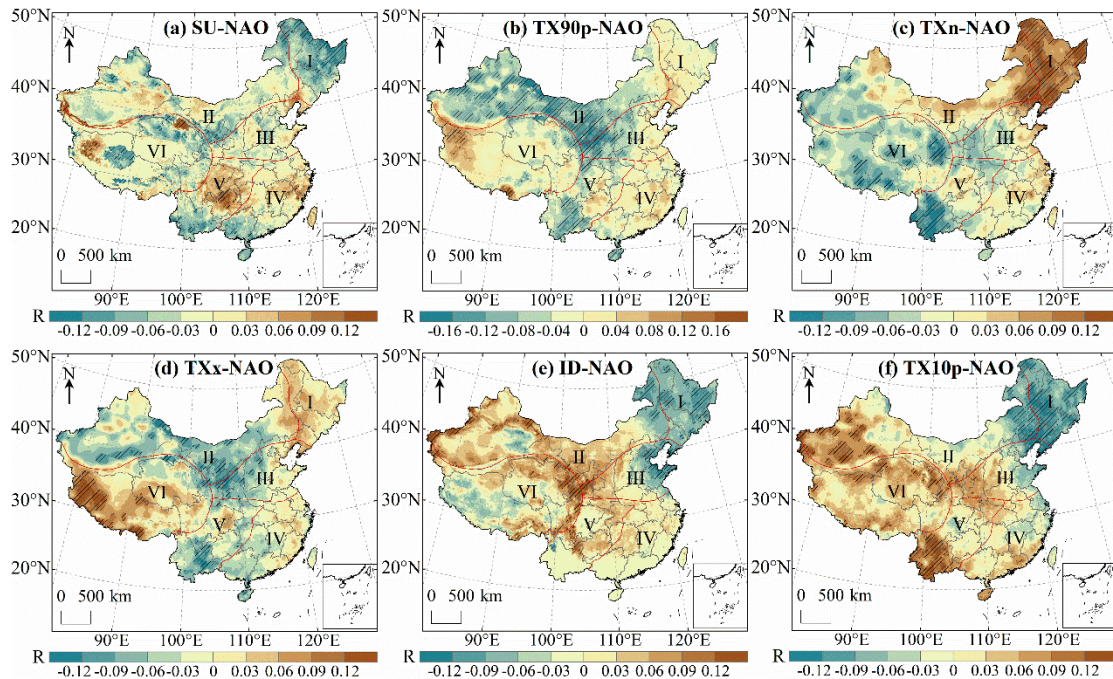


550

551 **Figure 16.** Correlation analysis between extreme temperature indices and IOBW in China during 1979–2018. The
 552 shaded areas indicate correlations that are significant at the 0.05 level.

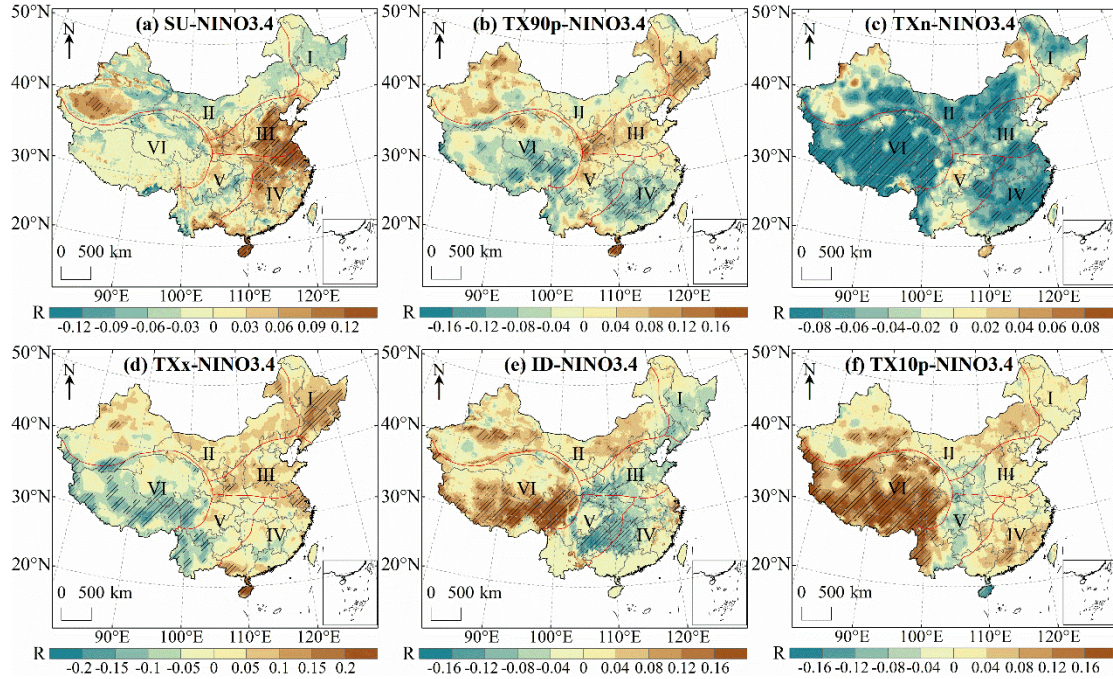
553 The influence of NAO on the extreme temperature indices is shown in Fig.17 (a-f). SU, TX90p,
 554 TXx and TXn were negatively correlated with the NAO more than they were positively correlated
 555 with NAO, indicating that the positive phase of NAO would lead to the decline of SU, TX90p, TXx
 556 and TXn over most of China. SU and NAO had a significant positive correlation in southern
 557 Xinjiang, western Tibet, northern Qinghai and northern Guizhou, but the correlation was very weak
 558 ($R < 0.2$). There was no significant correlation between SU and NAO in southern Qinghai, which
 559 was consistent with previous observations (Ding et al., 2018). The region with the strongest negative
 560 correlation between SU and NAO was located in Tibet ($R = -0.18$) (Fig. 17a). TX90p had a weak
 561 negative correlation with NAO in eastern Xinjiang ($R = -0.22$, $P < 0.01$). TX90p was significantly
 562 positively correlated with NAO in the west and south of region VI, but the correlation was extremely
 563 weak (Fig. 17b). Shi et al. (2019) indicated that more regions had a significant positive correlation
 564 between TXn and NAO in China than had a significant negative correlation, which was consistent

565 with our results. The areas of TXn had a significant positive correlation with NAO were mainly
 566 distributed in northeast China, while the regions with significant negative correlation were mainly
 567 located in central Tibet, eastern Qinghai and Yunnan (Fig. 17c). The correlation coefficient between
 568 TXx and NAO varied from -0.16 to 0.21. The regions with significant positive correlation between
 569 TXx and NAO were mainly located in Tibet, and the region with the strongest correlation was
 570 located in southern Tibet (Fig. 17d). The areas of ID was significantly positively correlated with
 571 NAO accounted for 5.86% of the whole study area, and the strongest correlation was found in
 572 western Xinjiang (R=0.23). The regions with significant negative correlation between ID and NAO
 573 were mainly distributed in eastern and northeastern China (Fig. 17e). Sun et al. (2016) found a very
 574 weak positive correlation between TX10p and NAO in the Loess Plateau, which was consistent with
 575 our results. The regions with a significant negative correlation were mainly concentrated in
 576 northeastern China (Fig. 17f).



577
 578 **Figure 17.** Correlation analysis between extreme temperature indices and NAO in China during 1979-2018. The
 579 shaded areas indicate correlations that are significant at the 0.05 level.

580 Fig.18 (a-f) shows the correlation between NINO3.4 and extreme temperature indices. The
581 regions with significant positive correlation between SU and NINO3.4 were mainly distributed in
582 eastern China, indicating that the events of El Niño would lead to an upward trend of SU in these
583 regions. There were few regions with significant negative correlation between SU and NINO3.4,
584 only accounting for 1.15% of the entire research area, mainly distributed in southeast Tibet and
585 southwest Yunnan (Fig. 18a). The correlation coefficient between TX90p and NINO3.4 was -0.19-
586 0.26. The areas of TX90p had a significant negative correlation with NINO3.4 were mainly
587 distributed in region IV and VI (Fig. 18b). There was a significant negative correlation between
588 TXn and NINO3.4 in 24.59% of regions, and the region with the strongest negative correlation was
589 located in Tibet ($R=-0.25$). TXn was positively correlated with NINO3.4 in only 10.46% of regions
590 in China, and the region with the largest correlation coefficient was northwest Xinjiang ($R=0.11$)
591 (Fig. 18c). There was a weak positive correlation between TXx and NINO3.4 in southern
592 Guangdong and northern Hainan ($0.2 < R < 0.4$). The regions of TXx was significantly negatively
593 correlated with NINO3.4 were mainly distributed in the south of region V and region VI (Fig. 18d).
594 The significant negative correlation between ID and NINO3.4 was mainly concentrated in southern
595 China. The areas with significant positive correlation were mainly distributed in the western region
596 II and southern region VI, and the region with the strongest correlation was located in the western
597 Sichuan ($R=0.31$) (Fig. 18e). TX10p in most regions of regional VI was significantly affected by
598 NINO3.4, and the significant positive correlation area accounted for 69.31% of the whole region VI.
599 TX10p was significantly negatively correlated with NINO3.4 in only 0.65% of regions in China,
600 mainly distributed in Hainan and southern Gansu (Fig. 18f).



601

602 **Figure 18.** Correlation analysis between extreme temperature indices and NINO3.4 in China during 1979-2018.

603

The shaded areas indicate correlations that are significant at the 0.05 level.

604

7 Conclusions

605

The global temperature continues to rise and extreme weather events continue to increase (IPCC,

606

2021). It is great significance to study regional high temperature changes. In order to obtain the key

607

parameters of high temperature spatial-temporal variation analysis, this study proposed a daily T_{\max}

608

estimation frame based on the near-surface T_a grid data and T_a diurnal variation model to build a

609

T_{\max} dataset in China from 1979 to 2018. Validation of T_{\max} estimation data in six natural regions

610

indicated that the RMSE of each region was between 2.38-2.94°C, the MAE was between 1.88-

611

2.45°C, and R^2 was between 0.95-0.99. After using the regression model to calibrate the dataset, the

612

accuracy of the estimated T_{\max} has been significantly improved. The RMSE of the T_{\max} after

613

calibration reduced to 1.14-1.81°C, and the MAE reduced to 0.84-1.38°C, and the R^2 increased to

614

0.97-0.99.

615 This dataset was used to study the spatial-temporal variation characteristics of T_{\max} and the
616 corresponding influencing factors in China, and to discuss the correlation between T_{\max} , extreme
617 temperature indices and ocean climate modal indices. T_{\max} in all regions of China exhibited an
618 upward trend from 1979 to 2018, with the largest rise in region V and the smallest rise in region I.
619 In spring, T_{\max} in China increased significantly in most regions, and the region III is with the fastest
620 rising speed. In winter, T_{\max} in China had the least significant rise, and the region II was with the
621 slowest rise rate. SU, TX90p and TXx in all regions showed an upward trend. Except for region II,
622 TXn in other regions also exhibited an upward trend, while ID and TX10p in all regions showed a
623 downward trend. All extreme temperature indices had abrupt changes during 1979-2018, and most
624 of the abrupt changes occurred in El Niño or La Niña years. The region with the largest increase of
625 SU, TX90p and TXx and the region with the largest decrease of TX10p were located in the western
626 Yunnan. The correlation analysis between T_{\max} and extreme temperature indices and ocean climate
627 modal indices indicated that the increase of the IOBW usually coincides with the increase of T_{\max} ,
628 SU, TX90p, TXn and TXx and the decrease of ID and TX10p. NAO had the opposite relationships.
629 In most regions of China, T_{\max} , SU, TX90p and TXn were negatively correlated with NINO.3.4,
630 while TXx, ID and TX10p were positively correlated with NINO.3.4.

631 The T_{\max} dataset we produced can not only be used as the input parameters of climate change
632 models, crop growth models and carbon emission models, but also can be used to evaluate the risk
633 of high temperature disasters, which has high practical value. Currently, due to the limitation of the
634 temporal and spatial scope of the basic data, we have only produced the dataset of China. If global
635 station data and temperature data can be obtained in the future, we can continue to produce T_{\max}
636 dataset on a global scale. The analysis of regional high temperature temporal and spatial changes

637 shows that the temperature changes in different regions of China are inconsistent, and the
638 mechanism that affects the temperature rise is different in different regions, and some regions are
639 highly correlated with ocean temperature changes. China is located in the eastern Eurasian continent
640 and the western Pacific Ocean. With the influence of the unique topography of the Qinghai-Tibet
641 Plateau, China's climate system is very complex. The temperature change in China is affected by a
642 combination of factors, and the ocean is only one of the factors affecting the temperature change in
643 China. Our study found that the influence of the ocean on China's temperature change is not
644 particularly strong, and we can continue to study the driving factors that have a strong impact on
645 China's climate change in the future. In order to strengthen environmental protection and control
646 temperature rise, and formulate reasonable carbon emission reduction measures, we need further
647 research in the future.

648

649 *Code and Data availability.* CMFD is available from the National Qinghai-Tibet Plateau Science
650 Data Center (<https://data.tpsc.ac.cn/>). ERA5 data can be obtained from Copernicus Climate Data
651 Store (<https://cds.climate.copernicus.eu/>). Meteorological station data is available by CMA National
652 Meteorological Information Center (<http://data.cma.cn/>). IOBW index can be accessed at the
653 National Climate Center of CMA (<http://cmdp.ncc-cma.net/cn/index.htm>), and NAO index and
654 NINO3.4 index are from the National Oceanic and Atmospheric Administration of the United States
655 (<https://psl.noaa.gov/data/climateindices/list/>). The daily highest air temperature dataset and code
656 can be downloaded at <https://doi.org/10.5281/zenodo.6322881> (Wang et al., 2021).

657

658 *Author contributions.* PW and KM proposed the goals and aims of the research. FM provided
659 supervision and scientific guidance for the research. PW and SF built the dataset production model.
660 PW wrote the paper. KM, ZQ, SMB, and MA revised the final manuscript.

661

662 *Competing interests.* The authors declare no conflicts of interest.

663

664 *Acknowledgements.* The authors thank the China Meteorological Administration for providing
665 IOBW index and the ground measurements data, the Institute of Tibetan Plateau Research, Chinese
666 Academy of Sciences for providing CMFD dataset, and the NASA Earth Observing System Data
667 and Information System for providing the DEM data. We also thank the National Oceanic and
668 Atmospheric Administration of the United States for providing the ocean climate modal indices and
669 the ECMWF for providing the climate reanalysis data.

670

671 *Financial support.* This work is supported by the Framework Project of APSCO Member States
672 (Global and key regional drought forecasting and monitoring) & National Key Research and
673 Development Program of China (2019YFE0127600), the Fundamental Research Funds for Central
674 Nonprofit Scientific Institution (1610132020014) and the Open Fund of the State Key Laboratory
675 of Remote Sensing Science.

676

677 **References**

678 Abdullah, A. M., Ismail, M., Yuen, F. S., Abdullah, S., and Elhadi, R. E.: The Relationship between
679 Daily Maximum Temperature and Daily Maximum Ground Level Ozone Concentration, Polish
680 Journal of Environmental Studies, 26, 517-523, <https://doi.org/10.15244/pjoes/65366>, 2017.
681 Basu, R.: High ambient temperature and mortality: a review of epidemiologic studies from 2001 to 2008,
682 Environmental health, 8, 40, <https://doi.org/10.1186/1476-069X-8-40>, 2009.

683 Benali, A., Carvalho, A. C., Nunes, J. P., Carvalhais, N., and Santos, A.: Estimating air surface
684 temperature in Portugal using MODIS LST data, *Remote Sensing of Environment*, 124, 108-121,
685 <https://doi.org/10.1016/j.rse.2012.04.024>, 2012.

686 Ding, Z. Y., Wang, Y. Y., and Lu, R. J.: An analysis of changes in temperature extremes in the Three
687 River Headwaters region of the Tibetan Plateau during 1961-2016, *Atmospheric Research*, 209, 103-
688 114, <https://doi.org/10.1016/j.atmosres.2018.04.003>, 2018.

689 Du, Q. Q., Zhang, M. J., Wang, S. J., Che, C. W., Ma, R., and Ma, Z. Z.: Changes in air temperature over
690 China in response to the recent global warming hiatus, *Journal of Geographical Sciences*, 29, 496-516,
691 <https://doi.org/10.1007/s11442-019-1612-3>, 2019.

692 Ephrath, J. E., Goudriaan, J., and Marani, A.: Modelling diurnal patterns of air temperature, radiation
693 wind speed and relative humidity by equations from daily characteristics, *Agricultural Systems*, 51,
694 377-393, [https://doi.org/10.1016/0308-521X\(95\)00068-G](https://doi.org/10.1016/0308-521X(95)00068-G), 1996.

695 Evrendilek, F., Karakaya, N., Gungor, K., and Aslan, G.: Satellite-based and mesoscale regression
696 modeling of monthly air and soil temperatures over complex terrain in Turkey, *Expert Systems with
697 Applications*, 39, 2059-2066, <https://doi.org/10.1016/j.eswa.2011.08.023>, 2012.

698 Fabiola, F. P. and Mario, L. S.: Simple air temperature estimation method from MODIS satellite images
699 on a regional scale, *Chilean Journal of Agricultural Research*, 70, 436-445,
700 <https://doi.org/10.4067/S0718-58392010000300011>, 2010.

701 Gasparrini, A. and Armstrong, B.: The impact of heat waves on mortality, *Epidemiology*, 22, 68-73,
702 <https://doi.org/10.1097/EDE.0b013e3181fdcd99>, 2011.

703 Gu, H. H., Yu, Z. B., Peltier, W. R., and Wang, X. Y.: Sensitivity studies and comprehensive evaluation
704 of RegCM4. 6.1 high-resolution climate simulations over the Tibetan Plateau, *Climate Dynamics*, 54,
705 3781-3801, <https://doi.org/10.1007/s00382-020-05205-6>, 2020.

706 Guan, Y. H., Zhang, X. C., Zheng, F. L., and Wang, B.: Trends and variability of daily temperature
707 extremes during 1960–2012 in the Yangtze River Basin, China, *Global and Planetary Change*, 124,
708 79-94, <https://doi.org/10.1016/j.gloplacha.2014.11.008>, 2015.

709 He, J., Yang, K., Tang, W. J., Lu, H., Qin, J., Chen, Y. Y., and Li, X.: The first high-resolution
710 meteorological forcing dataset for land process studies over China, *Scientific Data* 7, 1-11,
711 <https://doi.org/10.1038/s41597-020-0369-y>, 2020.

712 Hersbach, H., Bell, B., Berrisford, P., Hirahara, S., Horányi, A., Muñoz - Sabater, J., Nicolas, J., Peubey,
713 C., Radu, R., Schepers, D., Simmon, A., Soci, C., Abdalla, S., Abellan, X., Balsamo, G., Bechtold, P.,
714 Biavati, G., Bidlot, J., Bonavita, M., De Chiara, G., Dahlgren, P., Dee, D., Diamantakis, M., Dragani,
715 R., Flemming, J., Forbes, R., Fuentes, M., Geer, A., Haimberger, L., Healy, S., Hogan, R. J., Hólm,
716 E., Janisková, M., Keeley, S., Laloyaux, P., Lopez, P., Lupu, C., Radnoti, G., de Rosnay, P., Rozum,
717 I., Vamborg, F., Villaume, S., and Thépaut, J.-N.: The ERA5 global reanalysis, *Quarterly Journal of
718 the Royal Meteorological Society*, 146, 1999-2049, <https://doi.org/10.1002/qj.3803>, 2020.

719 Hoffmann, L., Günther, G., Li, D., Stein, O., Wu, X., Griessbach, S., Heng, Y., Konopka, P., Müller, R.,
720 Vogel, B., and Wright, J. S.: From ERA-Interim to ERA5: the considerable impact of ECMWF's next-
721 generation reanalysis on Lagrangian transport simulations, *Atmospheric Chemistry and Physics*, 19,
722 3097-3124, <https://doi.org/10.5194/acp-19-3097-2019>, 2019.

723 Hong, Y. and Ying, S.: Characteristics of extreme temperature and precipitation in China in 2017 based
724 on ETCCDI indices, *Advances in Climate Change Research*, 9, 218-226,
725 <https://doi.org/10.1016/j.accre.2019.01.001>, 2018.

726 IPCC: Weather and Climate Extreme Events in a Changing Climate, Cambridge University Press,
727 Cambridge, <https://doi.org/10.1017/9781009157896.013>, 2021.

728 Johnson, M. E. and Fitzpatrick, E. A.: A comparison of two methods of estimating a mean diurnal
729 temperature curve during the daylight hours, *Archiv für Meteorologie, Geophysik und*
730 *Bioklimatologie, Serie B*, 25, 251-263, <https://doi.org/10.1007/BF02243056>, 1977.

731 Khan, N., Shahid, S., Ismail, T. B., and Wang, X. J.: Spatial distribution of unidirectional trends in
732 temperature and temperature extremes in Pakistan, *Theoretical and Applied Climatology*, 136, 899-
733 913, <https://doi.org/10.1007/s00704-018-2520-7>, 2018.

734 Kleinert, F., Leufen, L. H., and Schultz, M. G.: IntelliO3-ts v1. 0: a neural network approach to predict
735 near-surface ozone concentrations in Germany, *Geoscientific Model Development*, 14, 1-25,
736 <https://doi.org/10.5194/gmd-14-1-2021>, 2021.

737 Li, L. C., Yao, N., Li, Y., Liu, D. L., Wang, B., and Ayantobo, O. O.: Future projections of extreme
738 temperature events in different sub-regions of China, *Atmospheric Research*, 217, 150-164,
739 <https://doi.org/10.1016/j.atmosres.2018.10.019>, 2019a.

740 Li, Q. X., Yang, S., Xu, W. H., Wang, X. L., Jones, P., Parker, D., Zhou, L. M., Feng, Y., and Gao, Y.:
741 China experiencing the recent warming hiatus, *Geophysical Research Letters*, 42, 889-898,
742 <https://doi.org/10.1002/2014GL062773>, 2015.

743 Li, Y. L., Han, W. Q., Zhang, L., and Wang, F.: Decadal SST variability in the southeast Indian Ocean
744 and its impact on regional climate, *Journal of Climate*, 32, 6299-6318, [https://doi.org/10.1175/JCLI-](https://doi.org/10.1175/JCLI-D-19-0180.1)
745 [D-19-0180.1](https://doi.org/10.1175/JCLI-D-19-0180.1), 2019b.

746 Lin, S. P., Moore, N. J., Messina, J. P., DeVisser, M. H., and Wu, J. P.: Evaluation of estimating daily
747 maximum and minimum air temperature with MODIS data in east Africa, *International Journal of*
748 *Applied Earth Observation and Geoinformation*, 18, 128-140,
749 <https://doi.org/10.1016/j.jag.2012.01.004>, 2012.

750 Luan, J. K., Zhang, Y. Q., Tian, J., Meresa, H. K., and Liu, D. F.: Coal mining impacts on catchment
751 runoff, *Journal of Hydrology*, 589, 125101, <https://doi.org/10.1016/j.jhydrol.2020.125101>, 2020.

752 McGree, S., Herold, N., Alexander, L., Schreider, S., Kuleshov, Y., Ene, E., Finaulahi, S., Inape, K.,
753 Mackenzie, B., Malala, H., Ngari, A., Prakash, B., and Tahani, L.: Recent changes in mean and
754 extreme temperature and precipitation in the Western Pacific Islands, *Journal of Climate*, 32, 4919-
755 4941, <https://doi.org/10.1175/JCLI-D-18-0748.1> 2019.

756 Ninyerola, M., Pons, X., and Roure, J. M.: A methodological approach of climatological modelling of
757 air temperature and precipitation through GIS techniques, *International Journal of Climatology*, 20,
758 1823-1841, [https://doi.org/10.1002/1097-0088\(20001130\)20:14<1823::AID-JOC566>3.0.CO;2-B](https://doi.org/10.1002/1097-0088(20001130)20:14<1823::AID-JOC566>3.0.CO;2-B),
759 2000.

760 Parton, W. J. and Logan, J. A.: A model for diurnal variation in soil and air temperature, *Agricultural*
761 *Meteorology*, 23, 205-216, [https://doi.org/10.1016/0002-1571\(81\)90105-9](https://doi.org/10.1016/0002-1571(81)90105-9), 1981.

762 Poudel, A., Cuo, L., Ding, J., and Gyawali, A. R.: Spatio - temporal variability of the annual and monthly
763 extreme temperature indices in Nepal, *International Journal of Climatology*, 40, 4956-4977,
764 <https://doi.org/10.1002/joc.6499>, 2020.

765 Ruml, M., Gregorić, E., Vujadinović, M., Radovanović, S., Matović, G., Vuković, A., Počuča, V., and
766 Stojčić, D.: Observed changes of temperature extremes in Serbia over the period 1961 – 2010,
767 *Atmospheric Research*, 183, 26-41, <https://doi.org/10.1016/j.atmosres.2016.08.013>, 2017.

768 Salman, S. A., Shahid, S., Ismail, T., Chung, E.-S., and Al-Abadi, A. M.: Long-term trends in daily
769 temperature extremes in Iraq, *Atmospheric Research*, 198, 97-107,
770 <https://doi.org/10.1016/j.atmosres.2017.08.011>, 2017.

771 Sathaye, J. A., Dale, L. L., Larsen, P. H., Fitts, G. A., Koy, K., Lewis, S. M., and de Lucena, A. F. P.:
772 Estimating impacts of warming temperatures on California's electricity system, *Global Environmental*
773 *Change*, 23, 499-511, <https://doi.org/10.1016/j.gloenvcha.2012.12.005>, 2013.

774 Seenu, P. Z. and Jayakumar, K. V.: Comparative study of innovative trend analysis technique with Mann-
775 Kendall tests for extreme rainfall, *Arabian Journal of Geosciences*, 14, 1-15,
776 <https://doi.org/10.1007/s12517-021-06906-w>, 2021.

777 Sehra, S. T., Saliccioli, J. D., Wiebe, D. J., Fundin, S., and Baker, J. F.: Maximum daily temperature,
778 precipitation, ultraviolet light, and rates of transmission of severe acute respiratory syndrome
779 coronavirus 2 in the United States, *Clinical Infectious Diseases*, 71, 2482-2487,
780 <https://doi.org/10.1093/cid/ciaa681>, 2020.

781 Sen, P. K.: Estimates of the regression coefficient based on Kendall's tau, *Journal of the American*
782 *Statistical Association*, 63, 1379-1389, <https://doi.org/10.2307/2285891> 1968.

783 Shen, S. H. and Leptoukh, G. G.: Estimation of surface air temperature over central and eastern Eurasia
784 from MODIS land surface temperature, *Environmental Research Letters*, 6, 045206,
785 <https://doi.org/10.1088/1748-9326/6/4/045206> 2011.

786 Shi, J., Cui, L. L., Wang, J. B., Du, H. Q., and Wen, K. M.: Changes in the temperature and precipitation
787 extremes in China during 1961–2015, *Quaternary International*, 527, 64-78,
788 <https://doi.org/10.1016/j.quaint.2018.08.008>, 2019.

789 Sun, W. Y., Mu, X. M., Song, X. Y., Wu, D., Cheng, A. F., and Qiu, B.: Changes in extreme temperature
790 and precipitation events in the Loess Plateau (China) during 1960–2013 under global warming,
791 *Atmospheric Research*, 168, 33-48, <http://dx.doi.org/10.1016/j.atmosres.2015.09.001>, 2016.

792 Sun, Y. J., Wang, J. F., Zhang, R. H., Gillies, R. R., Xue, Y., and Bo, Y. C.: Air temperature retrieval
793 from remote sensing data based on thermodynamics, *Theoretical and Applied Climatology*, 80, 37-48,
794 <https://doi.org/10.1007/s00704-004-0079-y>, 2005.

795 Tan, M. L., Samat, N., Chan, N. W., Lee, A. J., and Li, C.: Analysis of Precipitation and Temperature
796 Extremes over the Muda River Basin, Malaysia, *Water*, 11, 1-16, <https://doi.org/10.3390/w11020283>,
797 2019.

798 Tong, S. Q., Li, X. Q., Zhang, J. Q., Bao, Y. H., Bao, Y. B., Na, L., and Si, A. L.: Spatial and temporal
799 variability in extreme temperature and precipitation events in Inner Mongolia (China) during 1960–
800 2017, *Science of the Total Environment*, 649, 75-89, <https://doi.org/10.1016/j.scitotenv.2018.08.262>,
801 2019.

802 Urraca, R., Huld, T., Gracia-Amillo, A., Martinez-de-Pison, F. J., Kaspar, F., and Sanz-Garcia, A.:
803 Evaluation of global horizontal irradiance estimates from ERA5 and COSMO-REA6 reanalyses using
804 ground and satellite-based data, *Solar Energy*, 164, 339-354,
805 <https://doi.org/10.1016/j.solener.2018.02.059>, 2018.

806 Wang, X. X., Jiang, D. B., and Lang, X. M.: Extreme temperature and precipitation changes associated
807 with four degree of global warming above pre - industrial levels, *International Journal of Climatology*,
808 39, 1822-1838, <https://doi.org/10.1002/joc.5918>, 2019.

809 Wang, Y., Peng, D. L., Shen, M. G., Xu, X. Y., Yang, X. H., Huang, W. J., Yu, L., Liu, L. Y., Li, C. J.,
810 and Li, X. W.: Contrasting Effects of Temperature and Precipitation on Vegetation Greenness along

811 Elevation Gradients of the Tibetan Plateau, *Remote Sensing*, 12, 2751,
812 <https://doi.org/10.3390/rs12172751>, 2020.

813 Wloczyk, C., Borg, E., Richter, R., and Miegel, K.: Estimation of instantaneous air temperature above
814 vegetation and soil surfaces from Landsat 7 ETM+ data in northern Germany, *International Journal of*
815 *Remote Sensing*, 32, 9119-9136, <https://doi.org/10.1080/01431161.2010.550332>, 2011.

816 Wu, R. G., Yang, S., Liu, S., Sun, L., Lian, Y., and Gao, Z. T.: Northeast China summer temperature and
817 north Atlantic SST, *Journal of Geophysical Research*, 116, <https://doi.org/10.1029/2011JD015779>,
818 2011.

819 Yang, Z. Y., Shen, M. G., Jia, S. G., Guo, L., Yang, W., Wang, C., Chen, X. H., and Chen, J.: Asymmetric
820 responses of the end of growing season to daily maximum and minimum temperatures on the Tibetan
821 Plateau, *Journal of Geophysical Research*, 122, 278-287, <https://doi.org/10.1002/2017JD027318>,
822 2017.

823 Yoo, C., Im, J., Park, S., and Quackenbush, L. J.: Estimation of daily maximum and minimum air
824 temperatures in urban landscapes using MODIS time series satellite data, *ISPRS Journal of*
825 *Photogrammetry and Remote Sensing*, 137, 149-162, <https://doi.org/10.1016/j.isprsjprs.2018.01.018>,
826 2018.

827 You, Q. L., Kang, S. C., Aguilar, E., Pepin, N., Flügel, W.-A., Yan, Y. P., Xu, Y. W., Zhang, Y. J., and
828 Huang, J.: Changes in daily climate extremes in China and their connection to the large scale
829 atmospheric circulation during 1961–2003, *Climate Dynamics*, 36, 2399-2417,
830 <https://doi.org/10.1007/s00382-009-0735-0>, 2011.

831 Zhai, P. M., Yu, R., Guo, Y. J., Li, Q. X., Ren, X. J., Wang, Y. Q., Xu, W. H., Liu, Y. J., and Ding, Y.
832 H.: The strong El Niño in 2015/2016 and its dominant impacts on global and China's climate, *Acta*
833 *Meteorologica Sinica*, 74, 309-321. (In Chinese), <https://doi.org/10.11676/qxxb2016.049>, 2016.

834 Zhang, H., Da, Y. B., Zhang, X., and Fan, J. L.: The impacts of climate change on coal-fired power plants:
835 evidence from China, *Energy & Environmental Science*, 14, 4890-4902,
836 <https://doi.org/10.1039/D1EE01475G>, 2021.

837 Zhang, M., Du, S. Q., Wu, Y. J., Wen, J. H., Wang, C. X., Xu, M., and Wu, S. Y.: Spatiotemporal changes
838 in frequency and intensity of high-temperature events in China during 1961-2014, *Journal of*
839 *Geographical Sciences*, 27, 1027-1043, <https://doi.org/10.1007/s11442-017-1419-z>, 2017.

840 Zhang, P. F., Ren, G. Y., Xu, Y., Wang, X. L. L., Qin, Y., Sun, X. B., and Ren, Y. Y.: Observed changes
841 in extreme temperature over the global land based on a newly developed station daily dataset, *Journal*
842 *of Climate*, 32, 8489-8509, <https://doi.org/10.1175/JCLI-D-18-0733.1> 2019.

843 Zhao, B., Mao, K. B., Cai, Y. L., Shi, J. C., Li, Z. L., Qin, Z. H., Meng, X. J., Shen, X. Y., and Guo, Z.
844 H.: A combined Terra and Aqua MODIS land surface temperature and meteorological station data
845 product for China from 2003 to 2017, *Earth System Science Data*, 12, 2555-2577,
846 <https://doi.org/10.5194/essd-12-2555-2020>, 2020.

847 Zheng, X., Zhu, J. J., and Yan, Q. L.: Monthly air temperatures over Northern China estimated by
848 integrating MODIS data with GIS techniques, *Journal of Applied Meteorology and Climatology*, 52,
849 1987-2000, <https://doi.org/10.1175/JAMC-D-12-0264.1> 2013.

850 Zhong, K. Y., Zheng, F. L., Wu, H. Y., Qin, C., and Xu, X. M.: Dynamic changes in temperature extremes
851 and their association with atmospheric circulation patterns in the Songhua River Basin, China,
852 *Atmospheric Research*, 190, 77-88, <https://doi.org/10.1016/j.atmosres.2017.02.012>, 2017.

853 Zhou, B. T., Xu, Y., Wu, J., Dong, S. Y., and Shi, Y.: Changes in temperature and precipitation extreme
854 indices over China: Analysis of a high - resolution grid dataset, *International Journal of Climatology*,
855 36, 1051-1066, <https://doi.org/10.1002/joc.4400>, 2016.

856 Zhu, S. Y., Zhou, C. X., Zhang, G. X., Zhang, H. L., and Hua, J. W.: Preliminary verification of
857 instantaneous air temperature estimation for clear sky conditions based on SEBAL, *Meteorology and*
858 *Atmospheric Physics*, 129, 71-81, <https://doi.org/10.1007/s00703-016-0451-3>, 2017.

859 Zhu, W. B., Lú, A. F., and Jia, S. F.: Estimation of daily maximum and minimum air temperature using
860 MODIS land surface temperature products, *Remote Sensing of Environment*, 130, 62-73,
861 <http://dx.doi.org/10.1016/j.rse.2012.10.034>, 2013.

862